

# Experiment for cryogenic large-aperture intensity mapping: instrument design

Eric R. Switzer,<sup>a,\*</sup> Emily M. Barrentine,<sup>a</sup> Giuseppe Cataldo,<sup>a</sup> Thomas Essinger-Hileman<sup>b</sup>,<sup>a</sup> Peter A. R. Ade,<sup>b</sup> Christopher J. Anderson,<sup>a</sup> Alyssa Barlis<sup>b</sup>,<sup>a</sup> Jeffrey Beeman<sup>b</sup>,<sup>c</sup> Nicholas Bellis,<sup>a</sup> Alberto D. Bolatto<sup>b</sup>,<sup>d</sup> Patrick C. Breyse<sup>b</sup>,<sup>e</sup> Berhanu T. Bulcha,<sup>a</sup> Lee-Roger Chevres-Fernandez,<sup>f</sup> Chullhee Cho<sup>b</sup>,<sup>a</sup> Jake A. Connors,<sup>g</sup> Negar Ehsan,<sup>a</sup> Jason Glenn,<sup>a</sup> Joseph Golec,<sup>h</sup> James P. Hays-Wehle,<sup>a</sup> Larry A. Hess,<sup>a</sup> Amir E. Jahromi,<sup>a</sup> Trevian Jenkins,<sup>d</sup> Mark O. Kimball,<sup>a</sup> Alan J. Kogut,<sup>a</sup> Luke N. Lowe,<sup>a</sup> Philip Mauskopf,<sup>i</sup> Jeffrey McMahon,<sup>h</sup> Mona Mirzaei,<sup>a</sup> Harvey Moseley,<sup>j</sup> Jonas Mugge-Durum,<sup>d</sup> Omid Noroozian,<sup>a</sup> Trevor M. Oxholm<sup>b</sup>,<sup>k</sup> Tatsat Parekh,<sup>a</sup> Ue-Li Pen,<sup>l</sup> Anthony R. Pullen,<sup>e,o</sup> Maryam Rahmani<sup>b</sup>,<sup>a</sup> Mathias M. Ramirez,<sup>m</sup> Florian Roselli,<sup>n</sup> Konrad Shire,<sup>d</sup> Gage Siebert<sup>b</sup>,<sup>k</sup> Adrian K. Sinclair,<sup>i</sup> Rachel S. Somerville,<sup>o</sup> Ryan Stephenson,<sup>i</sup> Thomas R. Stevenson<sup>b</sup>,<sup>a</sup> Peter Timbie,<sup>k</sup> Jared Termini<sup>b</sup>,<sup>p</sup> Justin Trenkamp,<sup>q</sup> Carole Tucker,<sup>b</sup> Elijah Visbal,<sup>r</sup> Carolyn G. Volpert,<sup>d</sup> Edward J. Wollack<sup>b</sup>,<sup>a</sup> Shengqi Yang,<sup>e</sup> and L. Y. Aaron Yung<sup>b</sup>,<sup>a</sup>

<sup>a</sup>NASA Goddard Space Flight Center, Greenbelt, Maryland, United States

<sup>b</sup>Cardiff University, Department of Physics and Astronomy, The Parade, Cardiff, United Kingdom

<sup>c</sup>Lawrence Berkeley National Laboratory, Berkeley, California, United States

<sup>d</sup>University of Maryland, Department of Astronomy and Joint Space-Science Institute, College Park, Maryland, United States

<sup>e</sup>New York University, Center for Cosmology and Particle Physics, Department of Physics, New York, United States

<sup>f</sup>University of Puerto Rico, Mayagüez, Puerto Rico, United States

<sup>g</sup>National Institute of Standards and Technology, Boulder, Colorado, United States

<sup>h</sup>University of Chicago, Department of Physics, Chicago, Illinois, United States

<sup>i</sup>Arizona State University, School of Earth and Space Exploration, Department of Physics, Phoenix, Arizona, United States

<sup>j</sup>Quantum Circuits, New Haven, Connecticut, United States

<sup>k</sup>University of Wisconsin Madison, Department of Physics, Madison, Wisconsin, United States

<sup>l</sup>Canadian Institute for Theoretical Astrophysics, Toronto, Ontario, Canada

<sup>m</sup>University of Arizona, Tucson, Arizona, United States

<sup>n</sup>ISAE-SUPAERO, Toulouse, France

<sup>o</sup>Flatiron Institute, Center for Computational Astrophysics, New York, United States

<sup>p</sup>University of Iowa, Iowa City, Iowa, United States

<sup>q</sup>Iowa State University, Ames, Iowa, United States

<sup>r</sup>University of Toledo, Department of Physics and Astronomy, Toledo, Ohio, United States

**Abstract.** The experiment for cryogenic large-aperture intensity mapping (EXCLAIM) is a balloon-borne telescope designed to survey star formation in windows from the present to  $z = 3.5$ . During this time, the rate of star formation dropped dramatically, while dark matter continued to cluster. EXCLAIM maps the redshifted emission of singly ionized carbon lines and carbon monoxide using intensity mapping, which permits a blind and complete survey of emitting gas through statistics of cumulative brightness fluctuations. EXCLAIM achieves high sensitivity using a cryogenic telescope coupled to six integrated spectrometers employing kinetic inductance detectors covering 420 to 540 GHz with spectral resolving power  $R = 512$  and angular resolution  $\approx 4$  arc min. The spectral resolving power and cryogenic telescope allow

\*Address all correspondence to Eric R. Switzer, [eric.r.switzer@nasa.gov](mailto:eric.r.switzer@nasa.gov)

the survey to access dark windows in the spectrum of emission from the upper atmosphere. EXCLAIM will survey 305 deg<sup>2</sup> in the Sloan Digital Sky Survey Stripe 82 field from a conventional balloon flight in 2023. EXCLAIM will also map several galactic fields to study carbon monoxide and neutral carbon emission as tracers of molecular gas. We summarize the design phase of the mission. © 2021 Society of Photo-Optical Instrumentation Engineers (SPIE) [DOI: [10.1117/1.JATIS.7.4.044004](https://doi.org/10.1117/1.JATIS.7.4.044004)]

**Keywords:** Galaxy formation; integrated spectrometers; low-temperature detectors.

Paper 21051 received Apr. 30, 2021; accepted for publication Nov. 1, 2021; published online Dec. 9, 2021.

## 1 Mission Overview

### 1.1 Science Goals in Context

The first luminous objects in the universe emerged in slowly coalescing gas clouds as early as ~200 million years after the big bang. Fueled by the condensation of matter and a constant supply of cold gas, the star formation rate across the universe increased<sup>1</sup> until it peaked at  $z \sim 2$ , commonly referred to as the cosmic high noon. Beyond this point, the cosmic star formation rate fell<sup>2</sup> ~10-fold to the present due to astrophysical processes, including several feedback mechanisms from stellar winds and active galactic nuclei that suppress star formation activities. The accelerated expansion of the universe appears to play only a minor role in the decline of star formation.<sup>3</sup> Measurements of the total molecular gas and the average conditions of the interstellar medium (ISM) are essential for refining galaxy evolution models throughout this critical period.

Conventional photometric surveys readily detect individual star-forming galaxies but may be limited in a census by selection effects and small field sizes. Selection effects can restrict access to numerous and typical galaxies that may be below detection limits, and rare bright objects are unlikely to appear in a small field. Small field sizes are subject to sample variance that limits the characterization of galaxy evolution at cosmological mean density. Additionally, optical and IR photometric surveys primarily access radiation from stellar populations in galaxies at rest-frame wavelengths too short to survey gas and dust content essential to understanding the ISM and precursors to star formation.

Line intensity mapping<sup>4,5</sup> is an emerging and complementary approach that probes the collective effects from bulk populations of galaxies in cosmologically large volumes. Line intensity mapping surveys the unresolved, integral surface brightness of redshifted line emission from galaxies. Line emission from a unique redshift maps to a specific frequency in the spectral survey. Specifically, the experiment for cryogenic large-aperture intensity mapping (EXCLAIM) will be able to detect CO and [CII] emission, which originate from warm and ionized molecular gas in the ISM and are good tracers for star formation activities.<sup>6,7</sup> Intensity mapping has parallels to measurements of the integrated far-IR background from COBE-FIRAS,<sup>8</sup> which supported decades of fruitful work resolving the background into its constituent galaxies.<sup>9</sup> Continuum dust emission dominates the far-IR background measured by COBE-FIRAS, so its spectrum has limited redshift information. In contrast, line intensity mapping measures the integral of line emission as a function of redshift, making it ideal for studying evolution. Large-area line intensity mapping surveys sensitive to dust and molecular gas will complement the James Webb Space Telescope, which will resolve individual galaxies to unprecedented depth in relatively small survey areas.

Balloon and satellite instruments are well-suited to enabling intensity mapping. First, the approach measures surface brightness (like the cosmic microwave background) rather than flux. Flux measurements require large apertures to achieve high sensitivity and reduce source confusion. In contrast, surface brightness measurements only need sufficient angular resolution to resolve cosmological scales of interest, keeping the instrument design focused on achieving high detector sensitivity rather than aperture size. Large aperture sizes are costly and challenging to implement in balloon and satellite applications. Next, intensity mapping measures the

cumulative emission of all sources over large volumes, allowing a blind, complete census. However, as a measure of cumulative emission, intensity mapping must rule out all sources of variance in the intensity from the Milky Way or line emission at other redshifts. Subject to these contaminants, cross correlation with a galaxy redshift survey provides a reliable way to extract information on average galaxy spectral energy distributions at target redshifts,<sup>10–14</sup> including both line and continuum emission.<sup>15</sup> Access to large volumes reduces sample variance, and cross-correlation approaches in the future may evade cosmic variance<sup>16–18</sup> or separate the integrated line signal into contributions of constituent galaxy populations and their halo membership.<sup>19</sup> Intensity mapping can employ multiple lines that trace different environments in the ISM. Further, because intensity mapping measures cosmological clustering, it is sensitive to star formation’s broader context in dark matter halos. Intensity mapping has applications in cosmological reionization, physical cosmology, and galaxy evolution.<sup>5</sup> Initial measurements of 21 cm, CO, [CII], and Ly- $\alpha$  emission through intensity mapping<sup>10,12–14,20–22</sup> have demonstrated its potential as an approach for studying galaxy evolution.

Traditional surveys of CO emission in individual galaxies suggest that molecular gas has fallen by a factor of six from  $z = 1.5$  to the present.<sup>2</sup> This decline accounts for only 20% of the stars formed since  $z = 1.5$ , so ongoing star formation requires neutral gas flows to replenish the molecular gas pool. Comparisons of these measurements to simulations of molecular gas<sup>23</sup> need an accounting of the finite field size and selection function of the galaxy survey. For example, based on the galaxies predicted by the Illustris-TNG<sup>24</sup> simulations, the ALMA-based ASPECS<sup>25</sup> survey has detected 70% of the overall CO emission at  $z = 1$ , declining to  $\sim 10\%$  at  $z > 2$ . Current simulations show molecular gas abundance roughly 10 times lower than observed when accounting for these effects. The small 4.6 arc min<sup>2</sup> field size of ASPECS results in sample variance that complicates the connection to simulations, especially at  $z < 1$ .

Intensity mapping approaches<sup>20–22</sup> for CO have provided constraints on the total Poisson variance of emission. Interpretation of this line autopower requires a model for emission in the CO ladder at all redshifts and ruling out other sources of variance in the emission. Cross correlation is critical to enabling the isolation of emission from a single line at a target redshift. An initial intensity mapping detection<sup>14</sup> of [CII] at  $z \approx 2.6$  in cross correlation between Planck 545 GHz data and the Baryon Oscillation Spectroscopic Survey (BOSS) quasar redshift sample suggests cumulative [CII] emission considerably higher than many models.<sup>26</sup> Current models<sup>27–29</sup> at these redshifts are anchored by or comparable to observations<sup>30</sup> of relatively few individual galaxies, often among the brightest of the population. There is considerable uncertainty within models<sup>26</sup> based on the range of their assumptions and between models, especially at the low-mass end of the population.

To proceed, EXCLAIM aims to conduct an intensity mapping survey of the integral emission from CO and [CII] over large areas and in cross correlation with well-defined spectroscopic galaxy redshift samples. These measurements will help rule out selection function and sample variance effects and tie the line emission to target redshifts. Additionally, measurements on large angular scales measure cosmological clustering from the halo context of galaxies.

This paper summarizes the design phase of the EXCLAIM mission. Unless described otherwise, numerical values are the current best estimates (CBEs) based on an analysis of the design. Measured values or citations describe inputs to the analysis in several systems. Future publications will describe more detailed science forecasts, spectrometer performance, and the instrument as-built and flown.

## 1.2 Overview of the EXCLAIM Survey

EXCLAIM is a balloon-borne telescope mission designed to map the spectrum from 420 to 540 GHz (714 to 555  $\mu\text{m}$ ) to constrain diffuse, integrated emission from several rotational ladder lines of CO ( $\nu_{\text{CO},N} = 115 N \text{ GHz}$  for  $J = N$  to  $J = N - 1$ ) in galaxies  $z < 1$  and [CII] ( $\nu_{\text{CII}} = 1.889 \text{ THz}$ ) in galaxies from  $z = 2.5$  to 3.5. The survey (Sec. 1.3.2) consists of a 320-deg<sup>2</sup> extragalactic field and several  $\sim 100$ -deg<sup>2</sup> Galactic regions.

EXCLAIM’s primary objective is cross correlation with the well-defined and large-area spectroscopic galaxy redshift surveys from BOSS.<sup>31</sup> Figure 1 shows constraints with expected EXCLAIM sensitivity relative to current models of CO<sup>22,32–39</sup> and [CII]<sup>27,37,40,41</sup> emission.

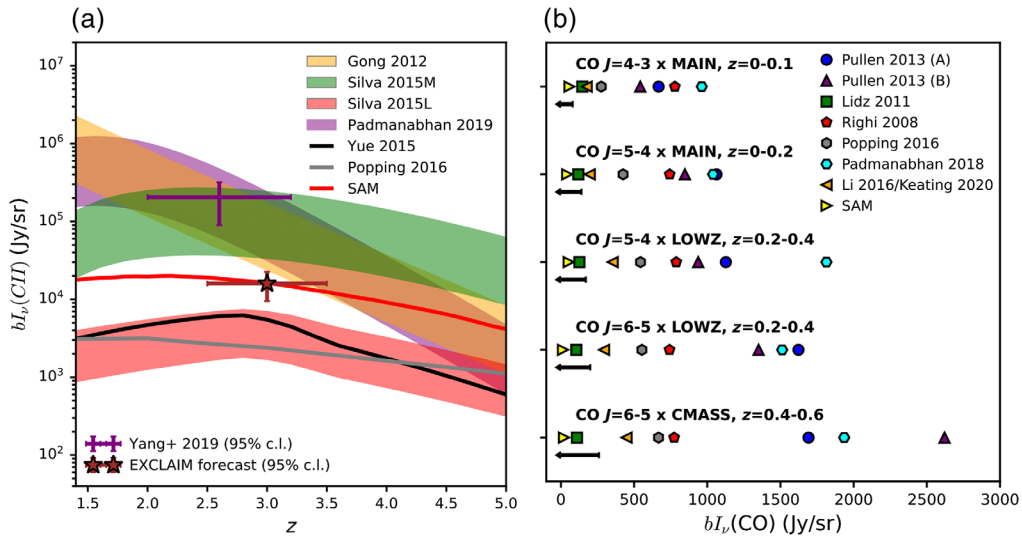


**Fig. 1** (a) Forecasts for the intensity at mean density times clustering bias ( $bI_v$ ) for [CII] in several models (described in the text). There is considerable variation within models (based on uncertainty in their parameters, indicated by bands) and between models based on their physical assumptions. An initial measurement with Planck 545 GHz (Yang+ 2019 above)<sup>14</sup> suggests high mean [CII] brightness, favoring collisional models of excitation. EXCLAIM is designed to definitively follow up this measurement. (b) Forecasts for CO in the redshifts and  $J$  ladder lines of CO that EXCLAIM will observe. Black arrows indicate EXCLAIM  $2\sigma$  upper limits, showing constraints on a range of models. MAIN, LOWZ, and CMASS label cross correlation with the BOSS galaxy samples.

In both figure panels, SAM refers to recent<sup>39</sup> semianalytic models<sup>42–44</sup> integrated over halos.<sup>45</sup> The collisional model<sup>40</sup> is modified to consider the density in halos<sup>28</sup> rather than average baryon density. For [CII], EXCLAIM aims to definitively follow up an initial detection of [CII] emission,<sup>14</sup> which pushes the limit of Planck 545 GHz data. EXCLAIM's data analysis will also evaluate the autopower in a path-finding capability. The cross-power measurement provides an estimate of the line power in the autopower, allowing a study of excess variance from foreground emission and instrumental effects.<sup>11,46</sup> EXCLAIM also acts as a pathfinder for the intensity mapping approach and integrated spectrometer design for future space mission applications.

The Galactic regions will observe neutral carbon ([CI], 492 GHz) and CO  $J = 4 - 3$  (460 GHz) in the Milky Way. [CI] traces gas phases that host  $H_2$  but where the CO tracer can be photodissociated, hence [CI] provides insight into how CO traces<sup>47,48</sup>  $H_2$ . We estimate the [CI] brightness by scaling<sup>49</sup> CO  $J = 1 - 0$  maps from the Planck mission<sup>50</sup> and find typical variations of  $\sim 10$  MJy/sr that are expected to be detectable with SNR  $\sim 10$  per beam.

The balloon float environment provides unique sensitivity and capabilities for the 420- to 540-GHz band. The high altitude results in low total atmospheric column depth and pressure broadening. The atmospheric emission resolves into narrow lines (Sec. 2.3), and spectrometry with resolving power  $R > 300$  can employ dark windows between lines where the photon loading (and so background-limited noise) is  $\approx 100\times$  darker than on bright lines and within a factor of  $\sim 6$  of the radiation background of space [As a rough order-of-magnitude, pressure broadening is  $\sim 10$  MHz/Torr and the spacing between bright lines is  $\sim 5$  GHz. To be in the wings of emission lines, down  $50\times$  their full-width at half-maximum (FWHM), requires  $< 10$  Torr or  $\sim 30$  km. The minimum spectral resolution to resolve (see between) these lines is  $R > 500$  GHz/5 GHz  $\sim 100$ .] Section 7.2 develops the parametric dependence of the sensitivity on  $R$  and shows that  $R = 512$  saturates the benefit of spectral resolution for EXCLAIM's parameter choices. Further, the parametric sensitivity to the tomographic intensity mapping signal scales as  $R^{0.35}$ , so it yields a diminishing benefit for higher spectral resolution. Optics at ambient temperature would dominate photon loading in the dark windows, so an all-cryogenic instrument is required to make full use of the low atmospheric brightness, accessing channels  $\approx 50\times$  darker than emission from an ambient temperature optic.

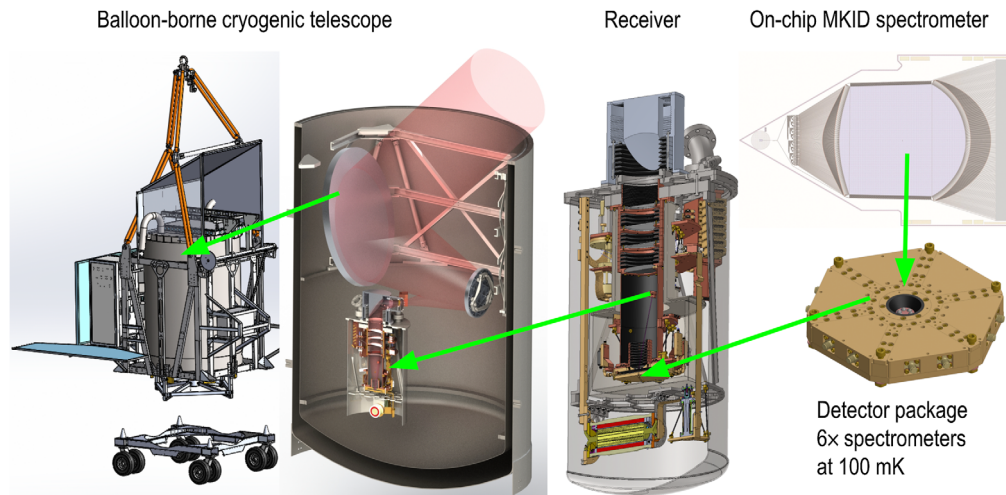


**Fig. 2** Overview of the EXCLAIM mission. EXCLAIM employs an all-cryogenic telescope design in a balloon platform to achieve low photon backgrounds. A focal plane maintained at 100 mK houses six integrated  $\mu$ -Spec spectrometers.

Figure 2 provides an overview of the mission and its technical approach. EXCLAIM maintains a fully cryogenic telescope (Sec. 2) and receiver (Sec. 4) in a 3000-l open bucket dewar with LHe, which has an interior 2-m deep and 1.5-m in diameter, following an approach from the ARCADE2 and primordial inflation polarization explorer (PIPER) instruments.<sup>51,52</sup> This is the maximum dewar size that stays within total payload mass limits of 3400 kg (Sec. 6.1). Superfluid fountain effect pumps<sup>53</sup> cool the optics to  $<5$  K and maintain the receiver at  $\approx 1.7$  K. The key enabling technology for the EXCLAIM mission is the  $\mu$ -Spec integrated spectrometer<sup>54–57</sup> (Sec. 3).  $\mu$ -Spec implements a Rowland spectrometer on a chip, which is coupled to kinetic inductance detectors (KIDs) and is designed for spectral resolving power  $R = 512$ . The primary mirror has a 75 cm projected diameter and yields an angular resolution  $\approx 4$  arc min (Sec. 2.2). The angular resolution works within the limitations of the balloon platform (Sec. 2.1.1) and is sufficient for resolving the transition from the clustering to shot-noise regimes in the line intensity signal. The large survey area provides access to the line clustering signal on linear scales, which traces the first moment of the luminosity function.

Several factors determined the EXCLAIM measurement band from 420 to 540 GHz. As primary science, EXCLAIM aims to validate and refine measurements of [CII] in Planck 545 GHz data in cross correlation with quasars.<sup>14</sup> The range 420- to 540-GHz provides good coverage of the Planck redshifts and corresponds approximately to the peak of the star formation rate density around which the mean [CII] emission is also expected to peak.<sup>27</sup> The 420- to 540-GHz band also provides access to  $J = 4 - 3$  and higher CO transitions near the peak of the CO spectral line energy distribution.<sup>58</sup> Operating near the emission peaks of CO and [CII] is beneficial in this first-generation detection instrument. From instrumental constraints, higher frequencies allow for smaller focal planes and yield a higher angular resolution. The Nb transmission lines in the spectrometer have a superconducting gap at  $\approx 680$  GHz, which limits the upper end of the operation in the current Nb/Al design. Design for a single spectrometer diffraction order simplifies the implementation (Sec. 3.1), and lower spectrometer orders provide sufficient bandwidth and good spectrometer performance. The band also avoids a bright ortho-water line at 557 GHz.

### 1.3 Survey Plan

#### 1.3.1 Fixing the telescope elevation

A cryogenic telescope frame inside the dewar fixes the observing elevation. (Throughout, elevation refers to the angle of the optical boresight relative to the horizon, and altitude refers to the balloon's altitude above sea level.) The fixed-elevation survey controls the modulation of the

atmospheric depth and stray light in the gondola. An implementation of elevation control would require either an enlarged exit aperture on the dewar (Sec. 2.1.1) and a cryogenic tilt mechanism (permitting only several degrees of movement) or mounting the dewar in an elevation cage (complicating management of the LHe volume). The survey scans in azimuth at a fixed elevation, allowing the sky to rotate through and following a mapping strategy used in instruments for the cosmic microwave background.<sup>59</sup>

EXCLAIM's primary extragalactic science employs cross correlation, and we prioritize access to the celestial equator due to a large number of available galaxy surveys.<sup>60</sup> Conventional flights from North America provide good access to these survey regions. Primary science is in cross correlation with the BOSS spectroscopic redshift catalog within the Stripe 82 (S82) region bounded by declination  $\pm 1.3$  deg and  $22\text{h}:24\text{ min} < \text{RA} < 4\text{h}:8\text{ min}$ . Additionally, Hyper Suprime-Cam (HSC) photometric redshifts<sup>61</sup> are available in this declination range and  $22\text{h} < \text{RA} < 2\text{h}:40\text{ min}$ , which will allow cross correlation with a much denser photometric catalog. Although HSC has a much higher number density of galaxies, photometric cross correlation will be a pathfinder rather than a baseline plan due to redshift uncertainties, the impact of which will take more time to quantify.<sup>62</sup> The equatorial field also overlaps with the Spitzer-HETDEX field<sup>63</sup> and the Herschel S82 survey.<sup>64</sup>

A survey fixed at 45 deg elevation provides a good balance between accessible sky below the celestial equator, atmospheric loading, and telescope design considerations. Access to the equator drives lower pointing elevation for higher flight geographic latitudes. A survey at 45 deg elevation can cover as far as 8 to 13.25 deg below the celestial equator, where 8 deg is from Four Corners, NM ( $\sim 37^\circ\text{N}$  latitude in northernmost flight from Fort Sumner, NM at  $34.5^\circ\text{N}$ ) and 13.25 deg is from Palestine, TX ( $31.75^\circ\text{N}$ ). This range covers many galaxy redshift surveys on the celestial equator and includes S82, even accounting for several-degree offsets in the pointing. Although an equatorial survey declination drives lower elevations, higher elevations yield lower atmospheric emission (2% per degree increase from nominal 45 deg) and less constraint on the telescope's geometry within the dewar, which has a fixed size. The balloon platform is limited to elevation  $< 66$  deg to minimize far sidelobe beam spill onto the balloon.

### 1.3.2 Survey strategy

The azimuth scan is determined by requirements to (1) cover the declination range of the S82 field and provide sufficient coverage for beam mapping, (2) sample the beam in 1/3 FWHM pixels in the sky drift and scan directions, and (3) work within the limitations of the attitude control system (Sec. 6.3). A sinusoidal scan executes the survey in azimuth with a 7 deg peak-to-peak throw and a period of 14 s. The sinusoidal scan limits abrupt movements that can excite higher harmonics in the flight train and gondola system. This scan covers  $\pm 1.4$  deg in declination around the celestial equator with a right ascension range determined by the survey duration.

Figure 3 shows a sample survey plan for a September 2022 Ft. Sumner flight. The survey starts with an elective daytime field (3 to 6 pm local) with an antisolar scan, covering  $200\text{ deg}^2$  in a stripe across the Galactic plane. Observing quality during the day is uncertain due to the Sun's potential to overwhelm detector response in the far sidelobes, which are difficult to model accurately. The first nighttime Galactic field will be observed with a scan across 35 deg to 42 deg azimuth from 6 to 7 pm local time and covering  $45\text{ deg}^2$ . The primary rising science field is observed from 7 pm to 1 am local time at 130 deg to 137 deg azimuth, covering  $305\text{ deg}^2$  of BOSS S82 (and overlapping with the HSC and HETDEX fall fields). Following the rising science field, the survey can reobserve the S82 field setting, move to a Galactic field, or mix both. The morning Galactic field covers 1 to 7 am local time in a scan  $-28$  deg to  $-35$  deg azimuth over  $220\text{ deg}^2$ . The setting science field covers 1 to 5:30 am local time in a scan  $-130$  deg to  $-137$  deg azimuth over  $224\text{ deg}^2$ . Moving to later times continues the S82 stripe into a Galactic region. We have identified a catalog of bright, nearby galaxies that can be observed in dedicated scans that slew out of the survey fields and will be planned before the flight. Section 7.3 describes the calibration and pointing model observations using planets and bright extragalactic sources in the science field. Overall, the rising S82 field provides 6 h of integration, and adding the setting field provides up to 10.5 h of integration on the S82 extragalactic region.

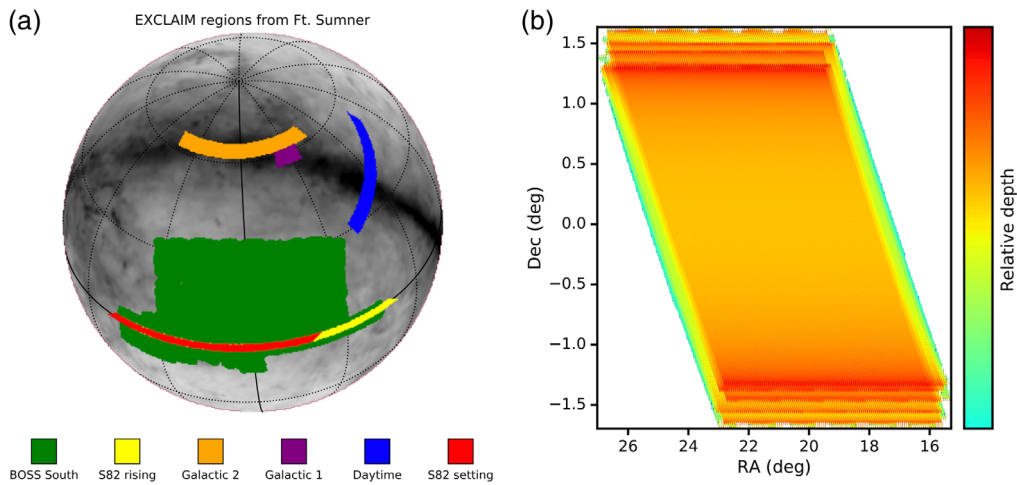


**Fig. 3** (a) Field coverage includes three opportunities for Milky Way surveys and rising and setting fields of BOSS-S82. (b) Scan depth in the S82 region for six spectrometers in a 30-min section of data.

## 2 Optical Systems

This section describes the EXCLAIM optical design. Section 7.2 describes the overall allocation of margins on stray light, angular resolution, and telescope efficiency.

### 2.1 Optical Design

#### 2.1.1 Telescope overview

EXCLAIM maximizes the cryogenic telescope aperture diameter in the cryogenic dewar volume (Fig. 4). The dewar drives the mass of the overall gondola (Sec. 6.1), which is currently within a reasonable margin of program limits. Lightweight dewar constructions and transfer approaches<sup>65</sup> could facilitate larger apertures in future missions. The optical envelope that determines the

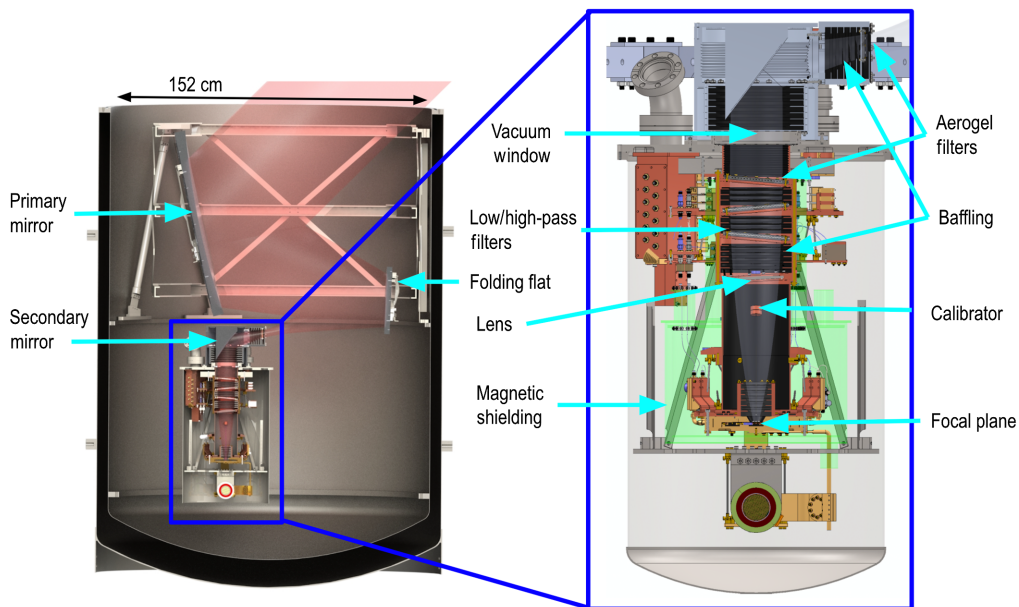


**Fig. 4** Overview of the EXCLAIM optical systems. The telescope, receiver, and supporting frames are lowered into a 3000-l LHe dewar. This design approximately maximizes the cryogenic aperture size allowed by this balloon architecture. All interfaces in the receiver must remain superfluid tight.

telescope design is 1.5-m deep and 1.2-m in diameter, is constrained to lie within a frame supported by bipod stands inside the dewar, and must account for the thickness of the optics and the optical mounts. The telescope has its boresight fixed at 45 deg elevation to conduct the survey (Sec. 1.3.1). We additionally require that the receiver remain vertical and be placed under the primary mirror to limit configuration changes in the receiver and readout umbilical (Sec. 4.4) during integration. The cryogenic readout section (Sec. 4.2) employs semirigid coaxial cables, which support a small translation from testing to flight configurations. The placement of the receiver in the dewar meets additional requirements that (1) LHe must not submerge the receiver window during science observation, (2) the LHe volume under the window must be sufficient for providing cryogenic hold time during the science operation (Sec. 6.5), and (3) the receiver must clear the bottom of the dewar and boiloff heater structures there. Within these constraints, the design employs a 90-cm parabolic primary mirror, 30-cm flat fold mirror, and 10-cm parabolic secondary mirror in an off-axis Gregorian configuration.<sup>66</sup> The primary mirror's effective focal length is 155 cm, giving an intermediate focus between the folding flat and the secondary mirror. The secondary mirror has an effective focal length of 19.5 cm, which produces a collimated input to the receiver.

### 2.1.2 Receiver optics

The window into the receiver is silicon with metamaterial antireflective (AR) surfaces<sup>67</sup> and has an open aperture 114-mm in diameter. The window thickness required to hold against atmospheric pressure is 9 mm. The baseline plan employs a laser-cut tapered AR layer<sup>68–70</sup> with <0.5% reflection across the band and an option for reversion to a more established process of a single, diced layer yielding <3.5% reflection. The metamaterial AR layer is implemented as a thin layer that is affixed to the pressure window. This facilitates manufacture and decouples the pressure window from the AR layer, which could introduce stress concentrations at its features. Kapton also presents a ready fallback. A quarter wavelength layer of Kapton is an appropriate AR coating for silicon, has a modest loss and well-understood adhesion,<sup>71</sup> and provides stock 75- $\mu\text{m}$  thickness that yields 15% loss in the band. A 27-cm collimated region in the receiver provides room for (1) magnetic shielding of the spectrometer package (Sec. 4.3), (2) baffling and a cold stop at an approximate image of the primary mirror for illumination control, (3) filters, tilted to control cavity modes, and (4) the receiver window and optical bench structure.

A plano-convex silicon lens with focal length 24 cm and metamaterial AR focuses light onto a focal plane with six integrated spectrometers (Sec. 3) along a 9-mm diameter. Section 3.1.2 describes the optical coupling onto the spectrometer. The plate scale is the ratio of focal lengths  $F_{\text{secondary}}/(F_{\text{lens}}F_{\text{primary}}) = 1.8$  arc min/mm and results in a modest 16.1 arc min total field of view for the 9-mm circle of spectrometers. A simple Gregorian design achieves a Strehl ratio >0.88 across the EXCLAIM band, avoiding the need for more complex design<sup>72,73</sup> approaches that would require an additional powered mirror.

Two polyimide aerogel filters loaded with diamond scattering particles act as low-pass filters with a cutoff of  $\sim 1$  THz.<sup>74</sup> High- and low-pass heat-pressed metal-mesh filters<sup>75</sup> define the band. Each detector in the spectrometer is sensitive to a bandwidth  $\Delta\nu \approx 0.9$  GHz, giving it a coherence length of  $c/\Delta\nu = 33$  cm. Since the filters and lens cannot be spaced multiple coherence lengths apart, they are tilted to avoid cavity modes and optical ghosts by terminating reflections in baffling. Filters are tilted by 2 deg and the lens is tilted by 3 deg. Each element is tilted at alternating angles to suppress cavity modes further. Section 3.1.2 describes the aggregate spectral response, which includes on-chip definition of the spectrometer diffraction order, and Fig. 5 shows the complete passband response.

### 2.1.3 Stray light control

The baseline design aims for total stray light due to thermal emission from the telescope to be <0.1 fW per spectrometer channel (measured at the cold stop) to maintain sensitivity near the photon background limit of dark windows in the upper atmosphere (Sec. 2.3). This translates into temperatures <5 K (at pessimistic 10% emissivity) in the reflective optics and <−40 dB total spill onto 250 K surfaces. Superfluid pumps cool the optics to 1.7 K.<sup>53,76</sup>

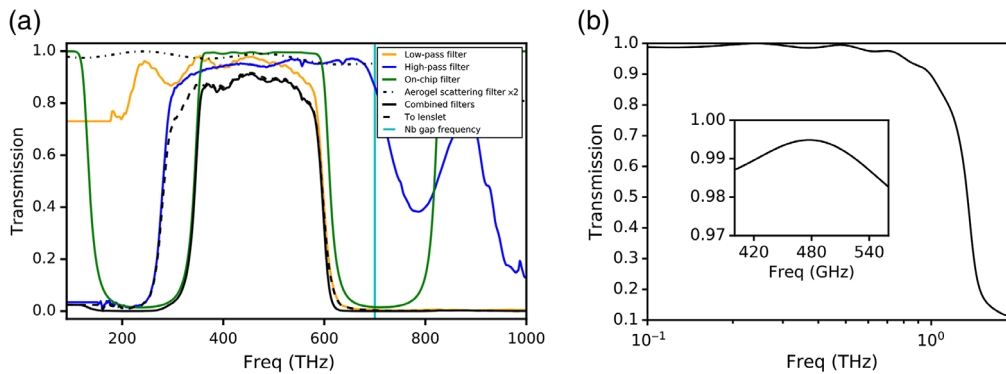


**Fig. 5** (a) EXCLAIM passband definition. Aerogel scattering filters block IR light, quasioptical filters define the input band of the spectrometer, and on-chip filters select the  $M = 2$  spectrometer order. (b) Modeled transmission versus frequency for a prototype aerogel scattering filter formulation for EXCLAIM. The inset shows modeled transmission in the EXCLAIM band, from 420 to 540 GHz. Band-averaged transmission is  $\sim 99\%$ .

To control the optical spill and maintain high aperture efficiency, a cold optical stop directly above the lens determines an edge taper of 15 dB in the lenslet response at the lowest EXCLAIM frequency of 420 GHz. Higher frequencies have a higher taper. The lenslet illumination of the stop is well-described by Gaussian optics. Section 2.2 describes diffraction analysis for the illumination on the primary. The stop's diameter is a free parameter and determines the Airy diffraction scale, and consequently the implied spill, of the primary mirror's illumination pattern. Conversely, several constraints drive a smaller stop based on the need to (1) maintain 3:1 aspect-ratio magnetic shielding (Sec. 4.6), (2) fit within the envelope of flight-like testing facilities (Sec. 4.7), and (3) control costs through modest filter and lens sizes. We find that a 7.4-cm stop diameter provides sufficient diffractive spill suppression within the envelope of competing requirements. The volume behind the cold stop houses a calibration emitter<sup>77</sup> in an integrating cavity that illuminates the spectrometer focal plane in a near sidelobe of the lenslet. It is used in calibration and characterization (Secs. 7.3 and 3.2.2).

Several groups of baffling control stray light: (1) a conical baffle and labyrinth at 100 mK manage stray light into the spectrometer package (Sec. 3.3), (2) a 1.7-K stop and baffling with inner diameter 7.6 cm in the collimated region truncate and control the primary mirror's illumination, (3) 1.7 K baffling surrounding the intermediate focus between secondary and primary mirrors limits acceptance angles for stray light into the receiver, and (4) feedthroughs control radiation from external interfaces to the receiver (Sec. 4.4.4). The  $f/1.5$  telescope optics determine the 10-cm diameter of collimated rays entering the receiver. The baffle assemblies are composed of a stack of metal rings with a 2-mm-thick molded<sup>78</sup> absorptive coating. This non-magnetic coating formulation<sup>79</sup> is a lossy dielectric mixture based on graphite-loaded epoxy with silica compensation to match the metal baffle's CTE appropriately.

## 2.2 Optical Model and Analysis

An analysis of physical optics is required to characterize the angular resolution and spill from each of the optics. We perform a diffractive analysis using POPPY<sup>80,81</sup> to assess spill on the primary mirror in the Fresnel regime and the far-field point spread function assuming on-axis optics. To assess the accuracy of the Fresnel limit in POPPY, we calculate a Fresnel number  $F$  accounting for powered optics.<sup>82</sup> For the critical region of propagation between the stop and the primary, we find  $F = 18.3$  within the near-field regime. We have also analyzed off-axis physical optics and astigmatism in Zemax, which finds a higher edge taper, even without baffling. Hence, the results from POPPY are more conservative. Figure 6 shows the results of the diffraction calculation and design that meets the  $-40$ -dB illumination requirement. Additionally, spill from the folding flat is controlled to  $-30$  dB, which is highly conservative based on temperatures  $< 10$  K measured in the PIPER dewar at these positions lower in the dewar than the primary

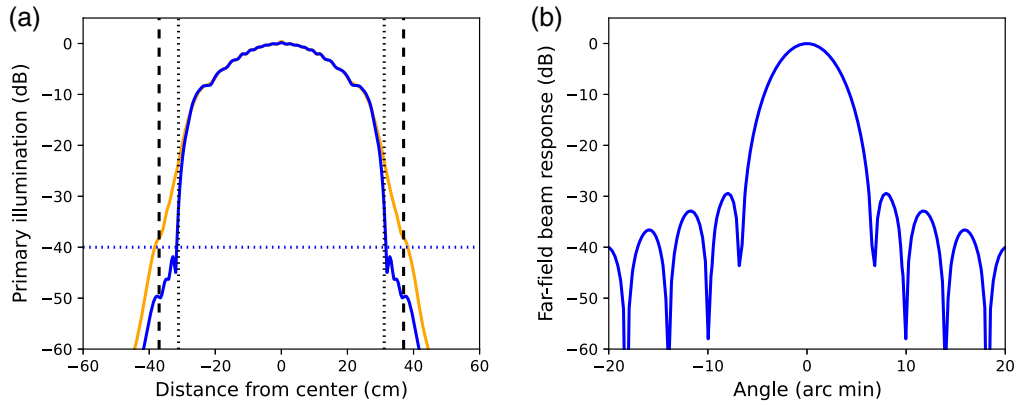


**Fig. 6** (a) An analysis of diffraction shows the illumination of the primary mirror at 420 GHz in a system without (yellow) and with (blue) optics tube baffling. The horizontal and vertical dotted lines show the required level of  $-40$  dB total solid angle spill and its position within the primary mirror, the envelope of which is shown by vertical dashed lines. This analysis shows that spill requirements are met at 420 GHz, the most stringent end of the band. (b) Far-field illumination pattern at 420 GHz as a result of the illumination on the primary mirror. The figure shows the illumination of a central spectrometer. The illumination pattern of each of the hexagon of spectrometers is offset 2 cm from this center.

mirror. The secondary mirror is surrounded by baffling, and the fold and primary mirrors are surrounded by absorbing guard rings that are cooled with superfluid pumps. In the far-field, the PSF has FWHM 4.86, 4.25, and 3.78 arc min for 420, 470, and 540 GHz, respectively. We additionally note that, at the nearest approach of the beams to the balloon, the  $-40$ -dB point is 5 m away from the boresight while the balloon is in the far sidelobes at 150 m.

### 2.3 Loading Model

Science forecasts use noise-equivalent intensity  $NEI = dI/dP(\nu) \cdot NEP(\nu)/\sqrt{2}$  (where  $\sqrt{2}$  converts  $1/\sqrt{\text{Hz}}$  in NEP to  $\text{s}^{1/2}$  in NEI), which requires a model for the NEP as a function of optical loading per channel  $P_{\text{opt}}(\nu)$  (Fig. 7), and the conversion from the intensity on the sky to power

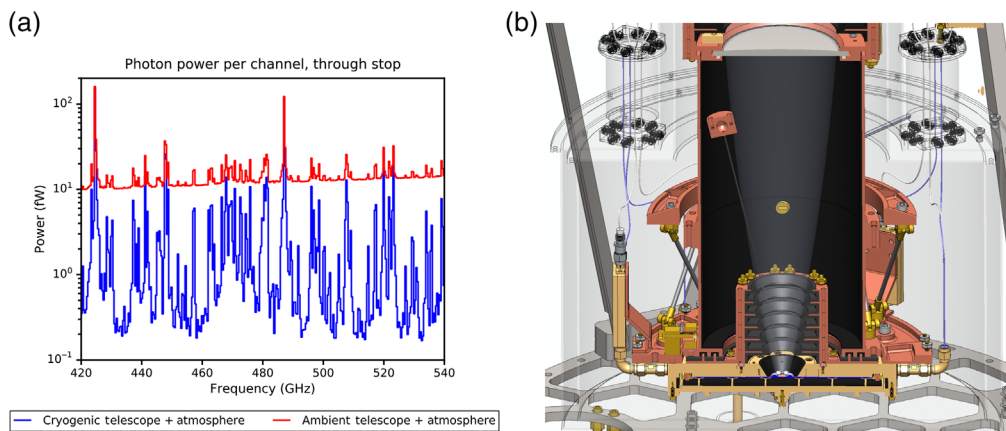


**Fig. 7** (a) The total optical loading per spectrometer channel, measured referring to total power through the stop. The photon loading is dominated by atmospheric emission, which resolves into narrow lines due to lower pressure broadening in the upper atmosphere. Also shown is the same model with cryogenic mirrors replaced by ambient temperature mirrors, motivating a cryogenic approach to accessing dark spectral channels in the upper atmosphere. (An ambient temperature window is not included here for simplicity but would add additional loading.) (b) Inset of the focal plane showing the bundle of rays that define power incident to the spectrometer from the stop.

$dP/dI$ . Throughout, optical powers refer to power through the cold stop, unless described otherwise. This definition of NEP applies to the integrated spectrometer performance (including efficiency) and is the quantity measured in blackbody load tests (Sec. 3.2.2).

We model loss in the silicon lens<sup>67,83</sup> and window with  $n = 3.39$ ,  $\tan \delta = 5 \times 10^{-6}$ , and 0.5% reflection per tapered AR layer surface. The overall receiver optics yield a 12.3% average estimated in-band loss. The primary and secondary mirrors each have negligible (0.4%) loss assuming  $1.2 \times 10^7$  S/m conductivity<sup>84</sup> (conservatively taking the value at 300 K) and tightly controlled spill. Atmospheric emission is calculated from a model<sup>85</sup> for a North American flight with 36 km altitude and 45 deg elevation. Atmospheric optical depth is negligible for the science channels. The model includes radiation in the  $M = 1$  and  $M = 3$  spectrometer diffraction orders (dominated by CMB radiation in  $M = 1$  and assuming no transmission above the Nb gap at 680 GHz in  $M = 3$ ). The input filter (Sec. 3.1.2) suppresses out-of-order radiation by approximately  $-34$  and  $-25$  dB over the relevant range of  $M = 1$  and  $M = 3$  orders. Section 3.1.2 describes the remaining out-of-band radiation handling in the spectrometer. We include 0.4 MJy/sr from the CIB monopole<sup>8</sup> and 0.75 MJy/sr typical Milky Way emission in the S82 extragalactic region. All cryogenic optics temperatures are 2.2 K in the model at LHe's superfluid point, as a worst case above the expected operation at 1.7 K. Because power is defined as the optical power passing through the stop, the antenna efficiency in getting through the cold stop is accounted for in the spectrometer efficiency model, and the loading model includes emission from the region around the stop. The power per channel is the integral of  $dP/d\nu$  over a sinc<sup>2</sup> spectral response for the  $R = 512$  spectrometer over one radiation mode and one polarization. On average across the band, efficiency through the telescope optics to the stop is 85% and  $dP/dI = 0.78$  aW sr/MJy.

## 2.4 Optomechanical Implementation

The optical design is optimized in Zemax and verified to be diffraction-limited across the EXCLAIM band. The total allocation of the wavefront error (WFE) to produce a Strehl ratio  $>0.8$  is  $<0.075\lambda$  at the band center (470 GHz). The nominal design maintains WFE  $0.04\lambda$ . Machining of monolithic aluminum primary and secondary mirrors requires a figure of  $25 \mu\text{m}$  ( $0.02\lambda$  at 470 GHz), which in quadrature across the two mirrors gives  $0.028\lambda$ . The RMS roughness must be below  $2 \mu\text{m}$  to maintain scattering  $< -40$  dB.

Simulation studies prescribe tolerance requirements on the optical placements. The primary, fold, and secondary mirrors must be constrained to  $\pm 0.04$  deg,  $\pm 0.1$  deg, and  $\pm 0.4$  deg (translating to  $\approx 0.5$  mm in each case). Mirror decenter limits are  $<1$  mm, and placements across optics are  $<3$  mm. The vertical separation from the focal plane to lens (defocus), lateral separation, and tilt must be controlled to 1 mm, 0.5 mm, and 0.25 deg (or 0.4 mm at the mount points), respectively. Section 4.5.1 describes the focal plane placement tolerance through the sub-K thermal isolation. In placing the quasioptical system's focal plane, the geometric focus is at the phase center of the lenslet coupling to the slot antenna on the spectrometer (Sec. 3.1.2), including the CTE relative to the ambient temperature design.

We will use a coordinate measurement arm (Romer Model 7520) to measure fiducial features in each optical element in the integrated assembly. The primary, fold, and secondary mirror-receiver assembly are positioned using a symmetric hexapod consisting of locking turnbuckles (Fig. 8). Using an analysis of the structure, we convert displacements from the target alignment into turnbuckle turns. PIPER used a similar approach and achieved 0.1 to 0.2 mm placements on the optics and 0.3 mm on the receiver, within requirements on EXCLAIM optics.

All structural components inside the dewar and the receiver shell are 304 stainless steel to manage thermal contraction in cryogenic operation. Under slow, uniform cooling, the cryogenic segment will contract self-similarly. The reflective optics are aluminum to achieve low optical loss, high thermal conduction, low mass, and ease of manufacture. Three tangential flexures (Fig. 8) take up differential contraction relative to stainless steel. The secondary mirror employs smaller tangential flexures to connect to the stainless steel receiver lid. The silicon lenses are held in copper frames with spiral springs to accommodate differential CTE.<sup>86</sup>

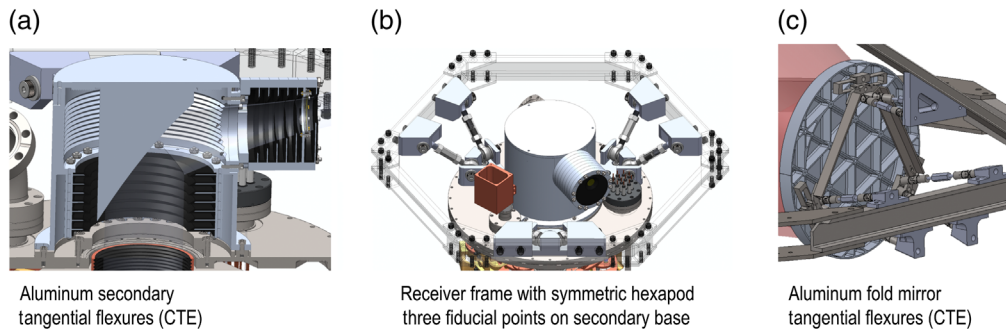


**Fig. 8** (a) The secondary mirror assembly is housed on the receiver lid and provides baffling in a collimated region and at the intermediate focus. (b) The receiver is positioned within the telescope frame using a symmetric hexapod of turnbuckles. All structural components are a common material (stainless steel) to avoid the effects of thermal contraction. (c) The primary, fold, and secondary mirrors are aluminum and employ a tangential flexure to accommodate thermal contraction. The primary and fold mirrors are positioned using hexapod turnbuckles.

### 3 Integrated Spectrometer

This section describes the  $\mu$ -Spec integrated spectrometer. Section 3.1 provides an overview, and Sec. 3.2 summarizes the overall performance expectations. Section 3.3 describes the package that houses the spectrometers, and Sec. 3.4 describes the ambient temperature readout.

#### 3.1 Spectrometer Design

##### 3.1.1 Overview

EXCLAIM employs a focal plane with six  $\mu$ -Spec spectrometers maintained at 100 mK.  $\mu$ -Spec implements a Rowland grating spectrometer with aluminum KIDs on a silicon chip (Fig. 9) using superconducting Nb microstrip planar transmission lines to transmit the signal and introduce the required phase delays.  $\mu$ -Spec provides an order of magnitude reduction in size compared with a free-space grating spectrometer, lithographic control of all components, high efficiency and

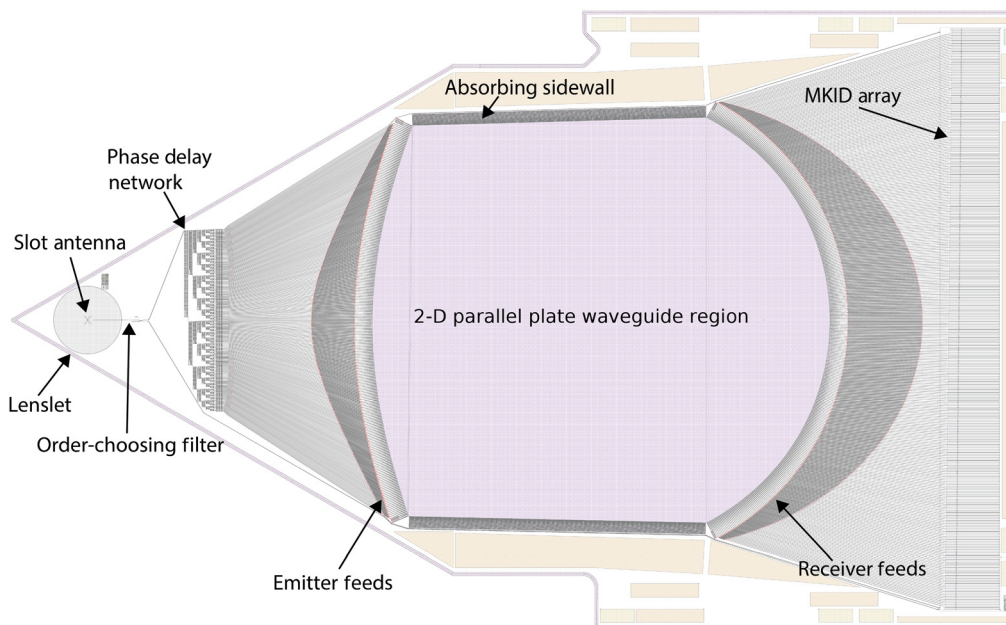


**Fig. 9** EXCLAIM employs the  $\mu$ -Spec integrated spectrometer, which implements all of the elements of a grating spectrometer lithographically on a 36 mm  $\times$  59 mm chip.

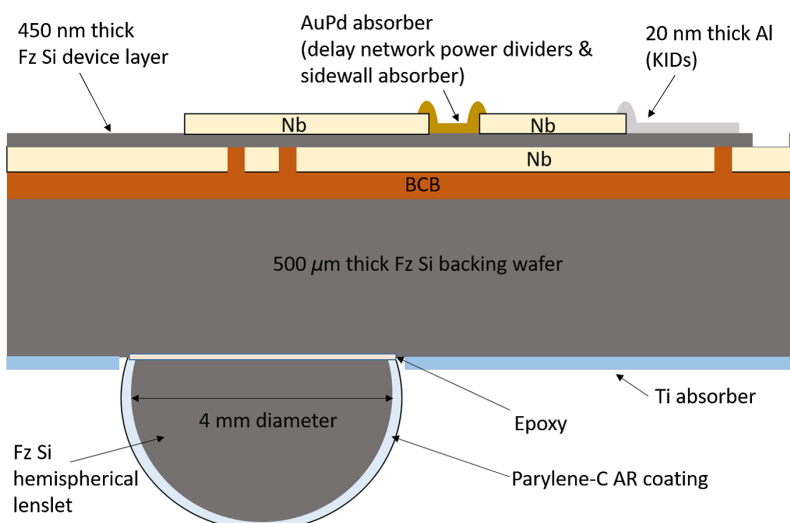


**Fig. 10** Cartoon cross section showing the layers of the EXCLAIM spectrometers, not drawn to scale.

resolution due to the low dielectric loss of single crystal silicon, and high immunity to stray light and crosstalk due to the microstrip architecture and thin dielectric (450-nm thick). Figure 10 shows a cross section of the spectrometer layers. We use KIDs due to their ease of fabrication, multiplexing capability, and ability to reach ultralow noise and high dynamic range.<sup>87</sup>

EXCLAIM uses a second-generation<sup>88</sup> design of  $\mu$ -Spec, customized for the 420- to 540-GHz band, a resolving power  $R = 512$ , and the optical loading conditions at balloon float altitude.<sup>89</sup> Table 1 summarizes performance parameters. This second generation follows a first-generation design and demonstration with resolving power  $R = 64$ .<sup>54–56</sup> A single spectrometer design with  $M = 2$  grating order covers the entire EXCLAIM band, eliminating the need for order-sorting filters<sup>90</sup> or a multi-order focal plane<sup>88</sup> while still providing a compact design, with six spectrometers fitting onto a single 150-mm diameter silicon wafer. Throughout, we use Ansys HFSS to simulate superconducting submillimeter and radio frequency (RF) components<sup>91</sup> and confirm with analytic limits. Integrated systems that are too large to simulate in HFSS employ custom numerical models.<sup>54</sup>

Light is coupled onto the chip using a dipole slot antenna, and a hyper-hemispherical silicon lenslet forms the beam that couples to the receiver optics (Sec. 3.1.2 and Sec. 2.1).  $\mu$ -Spec

**Table 1** EXCLAIM  $\mu$ -Spec spectrometer and KID design parameters.

Number of spectrometers	6
Spectrometer spectral band	420 to 540 GHz
Spectrometer grating order, $M$	2 (single order)
Spectrometer resolving power, $R$	512 at 472 GHz (center frequency) 535 to 505 over spectral band
Spectrometer efficiency	23%
KID NEP (at input to each KID)	$8 \times 10^{-19}$ W/ $\sqrt{\text{Hz}}$ at 0.16 fW (at KID) at 5 to 26 Hz acoustic frequency
Number of receivers/KIDs per spectrometer	355
KID readout band	3.25 to 3.75 GHz
Operating temperature	100 mK

synthesizes the diffraction grating with a binary tree of Nb microstrip transmission line meanders, which produce a linear phase delay and launch the light through  $N = 256$  emitting feeds into a 2D parallel plate waveguide region that acts as a spatial beam combiner. Along the receiving Rowland circle, 355 receiving feeds Nyquist sample the Airy spectral response and couple the light to Al KIDs. An absorber structure along the sidewall of the parallel plate waveguide region terminates reflections.

The resolving power  $R$  of an ideal spectrometer is the product of the number of emitters  $N$  and the grating order  $M$ , where  $R = N \cdot M$ . The EXCLAIM design provides  $R = 256 \cdot 2 = 512$  at the 470-GHz band center, with  $R = 535$  to 505 across the 420- to 540-GHz band. The emitting and receiving feeds in the 2D parallel plate waveguide region are a 2D analog of an adiabatic horn and couple to the Nb microstrip using a Hecken transformer.<sup>54</sup> The EXCLAIM design has a 10 $\times$  margin on the diffraction-limited grating spectrometer imaging criterion,<sup>92</sup> which requires that the delay from each channel in the grating has an RMS phase error of  $<2\pi/14$  rad. The emitter and receiver locations and transmission line lengths in the delay network are optimized to account for the frequency dependence of the phase velocity through (1) the Mattis–Bardeen penetration depth, (2) mutual inductance coupling between the adjacent straight microstrip segments in the delay network, and (3) phase velocity around the 180-deg miter bends in the delay network (confirmed by both analytical and HFSS modeling). The binary delay tree architecture nulls the effects of dispersion at the first order. For the microstrip geometry implemented, dispersion effects limit the design to a single grating order.

### 3.1.2 Optical coupling

The spectrometers are coupled through 4-mm-diameter hyper-hemispherical silicon lenslets with a 126- $\mu\text{m}$  Parylene-C AR coating. The lenslet is affixed to the supporting silicon backing wafer with epoxy and has an extension length of 675  $\mu\text{m}$  formed from the lenslet and backing wafer, maximizing directivity at 480 GHz. The slot antenna, lenslet, and AR layer are simulated in HFSS, and the thickness of the non-planar AR layer is numerically optimized. The lenslet has 8 deg FWHM in the mean of  $E$ - and  $H$ -plane responses at 470 GHz. Coupling efficiency through the cold stop is frequency-dependent (estimated as 73% at the 470-GHz band center), and we apply 60% coupling at 420 GHz estimated by HFSS as a conservative estimate at all frequencies. Accounting for 18% of light lost in the backing wafer and 1.5% in the AR coating<sup>93</sup> gives 49% optical coupling efficiency. We note that losses in the AR layer may be higher through the variation in measurements in the literature<sup>93,94</sup> and up to 9%. Section 7.2 allocates considerable contingency and margin on spectrometer efficiency to account for these and other uncertainties. Figure 10 shows several other layers traversed to reach the slot antenna, described in Sec. 3.1.4. The  $R = 64$  prototype demonstrated a thinned EpoTek-301 epoxy layer 0.5- $\mu\text{m}$  thick coupling the lenslet to the spectrometer, yielding an estimated  $2.5 \times 10^{-4}$  loss.<sup>95</sup> Maintaining negligible loss  $<1\%$  requires an epoxy layer  $<20 \mu\text{m}$ . Next, we estimate  $4 \times 10^{-5}$  loss crossing an SiO layer<sup>96</sup> of the backing wafer and  $6 \times 10^{-4}$  loss crossing the benzocyclobutene (BCB)<sup>97,98</sup> bond to the backing wafer.

The spectral band edges entering the spectrometer (Fig. 5) are determined primarily through an on-chip order-selecting filter that passes light with even spectral grating orders, with  $M = 0$  from 0 to 120 GHz,  $M = 2$  from 345 to 603 GHz, and  $M = 4$  plus higher even  $M$  orders ( $>820$  GHz). Additional free-space filters in the optics tube (Fig. 4) restrict input to the spectrometer's  $M = 2$  order. The 345- to 603-GHz passband into the spectrometer exceeds the spectral range from 420 to 540 GHz, and out-of-band radiation terminates on the sidewalls of the 2D parallel plate waveguide region, which have a return loss between 20 dB (normal incidence) and 35 dB (45 deg incidence typical for out-of-band radiation) through a planar metamaterial sidewall absorber.<sup>99</sup> Atmospheric emission in frequencies 300 to 420 GHz is passed by the filters and contributes 90% of the out-of-band stray light, equivalent to 0.7 fW per channel and falling on the sidewalls in the propagation region. In the worst case of normal incidence on the sidewalls and 20 dB attenuation, detector loading from this contribution is 25 $\times$  lower than the photon background in the darkest channels. The baseline loading model includes CMB monopole radiation in the  $M = 1$  (attenuated by the chip input filter) and  $M = 2$  (in-band) orders. CMB radiation outside the  $M = 1$  and  $M = 2$  orders is  $<0.06$  fW per channel and suppressed by  $>20$  dB

on the sidewalls. Additionally, power is expected to be smaller due to poorer optical coupling at lower frequencies. Although there are brighter atmospheric lines such as at 557 GHz, these are localized due to low-pressure broadening, and the total stray power is dominated by the band-average atmosphere and continuum sources.

All other components in the integrated spectrometer system have performance ranges exceeding EXCLAIM's science band. The slot antenna operates from 300 to 600 GHz and is modeled in parallel with the lenslet and AR layer for representative frequencies of 420, 470, and 540 GHz. The delay network and its power dividers operate from 300 to 600 GHz, the Hecken transformer operates  $>70$  GHz, and feed arrays operate from 300 to 1720 GHz (but in practice are limited by the 680-GHz Nb gap). The KIDs are sensitive to radiation  $>98$  GHz due to pair breaking above the superconducting energy gap determined by the 20-nm-thick Al superconducting transition temperature  $T_c = 1.33$  K. The delay network has right angle miter bends with  $-20$  dB coherent reflections. The length of the microstrip line between these bends is set to a fixed value to locate stop-bands at  $\sim 640$  GHz, above the EXCLAIM band.

### 3.1.3 KID detector design

The KIDs are resonators composed of two branches of a half-wave microstrip transmission line, which features a 20-nm-thick Al microstrip line over a Nb ground plane. The resonance frequencies span 3.25 to 3.75 GHz. Unlike titanium nitride superconducting films, Al films have been found to follow BCS theory<sup>100</sup> closely, simplifying design and analysis. In addition, by using a thin film, the kinetic inductance fraction is increased, and the effective volume is minimized, increasing KID sensitivity. Section 3.2 describes a performance model based on test device measurements. Except for the off-chip transition region of the RF readout feedline and narrow gaps near the coupling capacitor, an unbroken Nb ground plane protects the sensitive KIDs from stray light.

The array maintains a total RF bandwidth of 490 MHz, compatible with ROACH2 readout electronics.<sup>101</sup> We exclude resonators from a 2.678-MHz gap around the local oscillator at the center of the RF band and offset the first half of the array by  $1/2$  of a resonator spacing step to avoid image tones. The layout of the spectrometers on the wafer during fabrication is arranged such that the KIDs are approximately confined to a common radius, which helps control resonant frequency tolerance due to radial variations in film thickness. Measurements with a photomixer swept frequency source will provide each detector's optical spectral response regardless of their position in RF frequency. In addition to the 355 active detectors, there are also five dark or reference KIDs. A  $50 \Omega$  Al/Nb microstrip transmission line feeds the RF readout power to the KID array. A transition from microstrip to co-planar-waveguide (CPW) feedline at the output provides wirebonding access and has  $>29$  dB return loss. Ultimately, the wirebond connections between the spectrometer chips and an off-chip fanout board are likely to limit return loss for the feedline transmission at  $\geq 16$  dB.

At the KID RF readout frequencies, the optical input connections to the KIDs (coupling, transmission lines, and 2D parallel plate waveguide region) all appear as a short circuit and can be a source of spurious resonances. This effect was modeled, verified, and corrected in the  $R = 64$  prototype by maintaining the same interconnect length between the parallel-plate waveguide free-space region and each KID input and choosing a length to place any spurious resonances out of the RF readout band. This correction is also implemented in the EXCLAIM design with an equal length interconnect (of  $\sim 14$  mm) between the free-space region and the KIDs. This approach concentrates spurious modes in bands from 2.865 to 2.980 GHz and 4.774 to 4.966 GHz, which bracket but do not interfere with resonances in the 3.25-to 3.75-GHz readout band. Furthermore, the feedline width narrows near the region where it couples to the KIDs to compensate for the impedance of loading due to the resonators on the array, controlling the rotation of the resonators.

### 3.1.4 Fabrication

Fabrication follows a process developed in the  $R = 64$  prototype<sup>102,103</sup> to pattern the superconducting Nb and Al layers on both sides of a low-loss 450-nm single-crystal silicon device

layer of a 150-mm silicon-on-insulator wafer, using a flip-bonding process. The flip process bonds the device layer to a 500- $\mu\text{m}$ -thick float zone silicon backing wafer using BCB. We have implemented improvements in the Nb patterning process to address submillimeter and microwave loss issues discovered with the  $R = 64$  prototype devices and processes and modifications to realize submicron features now required in the slot antenna feed design.<sup>57</sup> In addition, the EXCLAIM spectrometers scale to a 150-mm-diameter wafer size (from the 100-mm-diameter wafers used for  $R = 64$  prototypes) due to the larger chip size of the higher resolution EXCLAIM spectrometer design and to maximize yield. In  $R = 64$  prototypes, it was found that both Al and Nb resonators had high microwave loss, determined to be due to two-level system (TLS) loss from an amorphous native oxide layer at the Nb ground plane and silicon interface, which impacted the performance of the KIDs. A modified Nb patterning process employs additional steps to remove native oxides and control sidewall profile and has yielded microwave  $Q_i \approx 150,000$  in diagnostic Nb films patterned into CPW resonator structures, in comparison with microwave  $Q_i \approx 8000$  in Nb CPW resonator structures patterned with the  $R = 64$  prototype process.<sup>57</sup> A wet-etch process patterns the Al and has yielded CPW devices with limiting  $Q_{i,0}^{-1} = 0.57 \times 10^{-6}$ . The backing wafer is patterned with a titanium layer to terminate stray light.

## 3.2 Performance and Requirements

### 3.2.1 Target performance for noise, efficiency, and spectral resolution

Estimates for dominant efficiency terms in the spectrometer are as follows: (1) lenslet coupling (49%), (2) order-choosing filter (98.7%), (3) planar region focal plane (50%, Fig. 11), (4) transmission lines (>94%), and (5) KID coupling (>99.4%). These contribute overall to a total  $\geq 23\%$  estimated design efficiency. This transmission line efficiency estimate assumes that there is no significant loss due to TLSs in amorphous oxides on the surfaces or interfaces of the superconducting Nb layer (and is addressed with modified Nb processing steps since the  $R = 64$  prototype, see discussion in Sec. 3.1.4) and that transmission line loss is dominated by the silicon dielectric loss with  $\tan \delta = 10^{-5}$  for high-purity silicon substrates.<sup>67,104,105</sup>

The spectral resolving power and efficiency are robust to worst-case impacts from loss in the Nb transmission lines. Summing the transmission  $|S_{21}|^2 = \exp(-2\pi L/\lambda/Q_i)$  (transmission line of length  $L$ ) over all emitters yields

$$R = MN_{\text{eff}} = M \sum_{n=0}^{N-1} \exp(-\pi Mn/Q_i) = M \frac{1 - \exp(-\pi MN/Q_i)}{1 - \exp(-\pi M/Q_i)}. \quad (1)$$

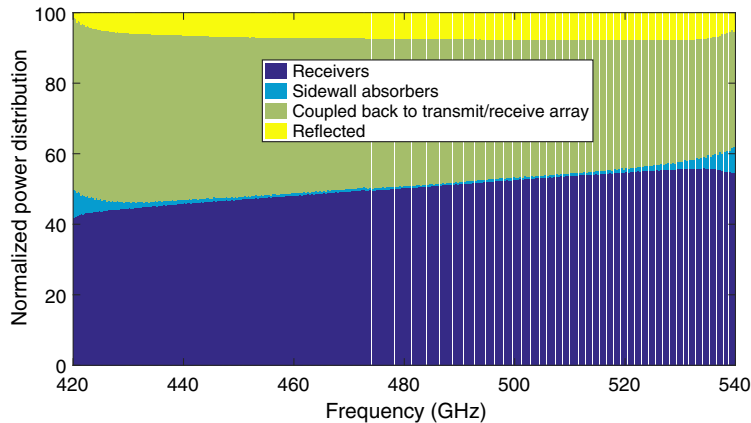


**Fig. 11** Efficiency in the 2D parallel plate waveguide region per detector, summing to unity for energy conservation. This breakdown accounts for return loss, isolation, and aperture efficiency and yields  $\approx 50\%$  efficiency coupling to the receiving array.

The measured spectral resolving powers of  $R = 64$  prototype devices are consistent with Nb transmission lines with submillimeter quality factors bound by  $Q_i > 5000$ . This worst-case transmission line loss results in  $R > 438$  ( $N_{\text{eff}} = 219$ ) in the EXCLAIM design. In addition, the fringe intensity is reduced by  $(N_{\text{eff}}/N)^2 = 73\%$ . New Nb film processes should yield improvements in Nb transmission line loss from  $R = 64$  prototype devices, and thus we expect a negligible impact on spectral resolving power and fringe amplitude. The transmission lines from the slot antenna to the delay network and the network's output to the ultimate KID optical input also contribute direct loss through 27 mm of total length. The worst-case  $Q_i > 5000$  and radiation wavelength  $\lambda = 173 \mu\text{m}$  in the microstrip results in  $>82\%$  worst-case transmission. Section 7.2 includes these worst-case losses as contingency in the overall sensitivity budget. We do not expect known fabrication tolerance to impact the resolution and estimate that  $R > 2300$  is achievable within  $2\pi/14$  rad RMS error, well over EXCLAIM's  $R = 512$ .

The resonators feature 20-nm-thick Al films and have a total volume of  $373 \mu\text{m}^3$ . Optical input to the KID is coupled to the middle of a half-wave resonator and generates quasiparticles across an absorption length of  $56 \mu\text{m}$ . For KIDs with illumination  $<40$  fW, quasiparticles are expected to diffuse throughout the entire branch length (3.4 mm). This limit applies to the channels on all but the brightest atmospheric emission lines (Fig. 7), which are highly down-weighted in the science analysis.

The noise model follows existing literature<sup>106</sup> with slight variations in the fitting forms described below. We calibrate the model based on measurements of the readout power and temperature dependence of quality factors, optical lifetimes, and homodyne noise in  $\approx 20$ -nm-thick Al CPW resonator test devices. Measured parameters for test resonators are reproducible from device to device on a single wafer and wafer to wafer over several-year time scales. The measured  $T_c$  for the films is 1.33 K and is consistent with expectations.<sup>107</sup> The kinetic inductance fraction, scaled from the CPW measurements to microstrip geometry, is  $\alpha = 0.78$ . Constant losses, not associated with the quasiparticles or TLSs, yield an inverse quality factor of  $Q_{i,0}^{-1} = 0.57 \times 10^{-6}$ . We find that TLS losses are well-described by dependence on temperature and readout power (through the number of readout photons  $N_{\text{photon}}$  in the resonator) as

$$\delta_{\text{TLS}} = \tanh\left(\frac{\hbar\omega_r}{2k_B T}\right) \frac{1}{\sqrt{N_{\text{photon}} + N_{\text{TLS}}}} \quad (2)$$

and yield  $Q_{i,\text{TLS}}^{-1} = 3.83 \times 10^{-5} \delta_{\text{TLS}}$  with  $N_{\text{TLS}} = 241$ . The TLS noise is empirically fit from homodyne noise measurements to have a two-sided frequency power spectrum  $S_{xx} = 1.5 \times 10^{-16} (f/1 \text{ kHz})^{-0.69} \delta_{\text{TLS}} \text{ Hz}^{-1}$ . We additionally find that the amplifier has gain fluctuations with spectral character similar to the TLS and increases  $1/f$  noise contributions by a factor of  $\approx 1.3$  in EXCLAIM's signal band. We believe that these gain fluctuations are related to an early generation low-noise amplifier (LNA) in the test setup, and they can be effectively removed in a common mode. The limiting lifetime at low temperature and read power in test devices is measured as 6 ms. Under EXCLAIM loading in the dark science channels and optimal read power,  $\tau_{\text{qp}} = 2.5$  ms will not be limited. Cumulative output chain noise referred to the LNA's input is measured as 4.1 K. We expect to use only the frequency quadrature in primary science.

Higher read tone powers suppress both amplifier and TLS noise, but tones can also stimulate quasiparticles or produce a non-linear response in the resonator, so they cannot be increased arbitrarily. From readout power sweeps, we find that the efficiency for readout power to generate quasiparticles is  $1.2 \times 10^{-3}$  per readout photon, allowing good management of the TLS and amplifier noise. We optimize the readout power across the KID array to give the minimum total NEP at each optical power across the EXCLAIM band. Although lower resonator volumes have higher responsivity, larger volumes yield longer lifetimes and a greater ability to control TLS noise using the readout power.

The optical loading varies over the band, resulting in significant NEP variations. Section 7.1 incorporates these variations into a figure of merit NEP for the full spectrometer, also incorporating its efficiency. As a single-point model for describing the performance of the KIDs, the optical loading in the science channels is 0.7 pW per channel (measured at the stop), corresponding to 0.16 pW at the KID. The noise-equivalent power (with power defined at the input to the

KID) is expected to be  $\text{NEP}_{\text{det}} < 8 \times 10^{-19} \text{ W}/\sqrt{\text{Hz}}$  at input powers of 0.16 fW and 5 to 26 Hz acoustic frequencies.

Cosmic rays must be cut from the data, which impacts the integration time. Recently, OLIMPO has measured cosmic ray rates<sup>108</sup> in a KID array at balloon float. Scaling the observed rate relative to the EXCLAIM spectrometer chip area predicts one cosmic ray hit per 20 s, resulting in a 0.3% loss for a worst-case 6 ms detector time constant. KIDs are less susceptible than transition-edge sensors to cosmic ray impacts because they are well heat-sunk to the bath and do not have isolated thermal islands.

### 3.2.2 Spectrometer characterization

The integrated spectrometer's NEP and efficiency will be characterized using a beam-filling blackbody integrated into the dilution refrigerator test facility (Fig. 12). Emission from the blackbody allows a determination of noise performance as a function of optical power and readout tone power and will simulate flight loading conditions. The aggregate spectrometer performance is characterized by an effective NEP (Sec. 7.1), which accounts for variations in performance with acoustic frequency and as a function of optical loading across the array. The blackbody is fabricated with a V-shaped design from COBE-FIRAS<sup>109</sup> to achieve  $< -35$  dB reflection using multiple bounces, is thermally isolated from the cold stage with carbon fiber tubes, and is enclosed by a 1-K intermediate stage. The path between the spectrometer and blackbody has quasi-optical filters with specifications identical to those in the receiver optics. The blackbody facility has a cryogenic iris, which allows for modulation of the source.

A photomixer swept line source allows for the characterization of each detector's frequency response, following an approach developed for the  $R = 64$  prototype device. The source has a frequency drift with operating temperature, so we also plan to use atmospheric and Galactic line emission at known frequencies and a silicon etalon to calibrate the absolute frequency scale. We will also instrument the calibration emitter with the blackbody tests to provide a transient signal and calibrate the emitter.

### 3.2.3 Requirements on operating conditions

The spectrometer imposes requirements on the sub-K cooling system, with operation  $< 125$  mK and stability  $< 20 \mu\text{K}/\sqrt{\text{Hz}}$ . Bath temperature exponentially activates quasiparticle generation, so effects of the bath temperature fall quickly toward a lower temperature. The stability requirement maintains temperature-induced KID signal fluctuations below the detector noise in a pessimistic scenario in which the effective quasiparticle temperature is 200 mK. Operation at  $< 125$  mK bath temperatures provides a margin for operation in a regime in which thermal generation is negligible. The thermal generation rate at 125 mK is  $10^6$  lower than 200 mK. Due to the exponential activation, the sensitivity of the KIDs to bath temperature variations also

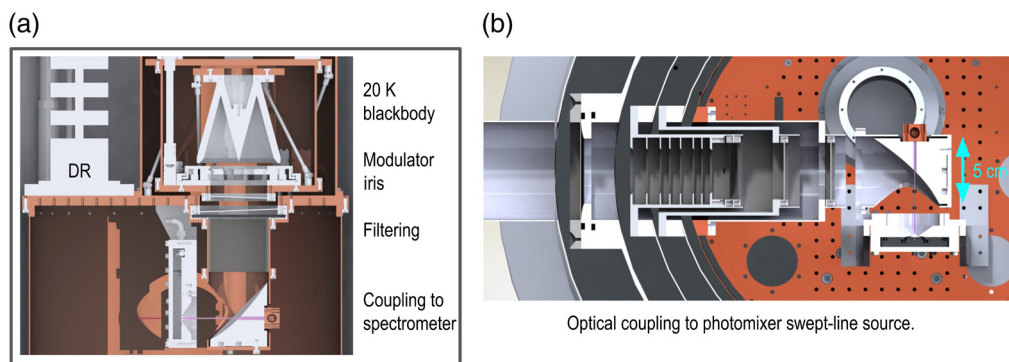


**Fig. 12** Spectrometer characterization facilities. (a) Beam-filling blackbody emitter for measuring efficiency and noise. (b) Swept frequency photomixer source coupling to characterize spectral response (employed in the  $R = 64$  prototype).

rapidly falls at lower temperatures. The requirement  $<20 \mu\text{K}/\sqrt{\text{Hz}}$ , including in long-term stability, is well within the demonstrated performance of the adiabatic demagnetization refrigerator (ADR)<sup>110</sup> and controller.<sup>76</sup>

At lower optical loads, the quasiparticle number density drops, and the quasiparticle lifetime increases. In the darkest atmospheric windows, we expect time constants of 2.5 ms, easily meeting the  $<23$ -ms requirement for time constants to sample the beam in the scan direction. The baffle region surrounding the intermediate focus (Sec. 2.1) can support a modulator if required to manage  $1/f$  noise. The baseline survey uses azimuthal scanning to modulate the science signal to the 5- to 26-Hz band (Sec. 7.1), where TLS noise is subdominant in test device noise measurements.

Magnetic field requirements are based empirically on shield configurations, which have yielded high quality factors in similar resonators. The Al line width is  $\sim 3 \mu\text{m}$ , so vortex trapping is not expected, but the Nb ground plane has the potential to trap vortices if not sufficiently shielded. Trapped vortices can respond to forces from microwave fields and dissipate energy, impacting performance. Previous  $R = 64$  Al KIDs and CPW Al and Nb test devices show no performance degradation in a single external mu-metal shield ( $\sim 25\times$  attenuation) or with this shield plus an internal Cryoperm shield. The receiver (Sec. 4.3) provides shielding estimated to be  $>10^4$ . The receiver's ADR is outside the shield region and is not magnetized until the stage temperature drops to 900 mK through precooling by a  $^4\text{He}$  adsorption refrigerator (Sec. 4.5), so it is below the  $T_c$  of both Al and Nb. In the absence of spectrometer shields, the stray fields from the ADR's shield are  $<5$  G.

### 3.2.4 Stray light control and crosstalk

A thin Ti coating deposited on the back side of the wafer (Fig. 10) controls light propagation in the backing wafer. The  $R = 64$  test device employed a similar absorbing layer and demonstrated attenuation of  $\sim 10^4$ , measured using dark KIDs in a configuration with and without the absorbing film. The backing wafer thickness of  $500 \mu\text{m}$  provides a balance between transmission cutoff, maximized bounces, and safe wafer handling. Additional coupling is controlled by minimizing the number of groundplane cuts to only those required in the slot antenna and the coupling capacitor regions.

Thermal blocking filters<sup>111</sup> at the RF readout input to the spectrometer package mitigate stray radiation introduced through the readout coaxial cable. Box-in-box architectures<sup>87,112</sup> have demonstrated upper limits on stray light  $<60$  aW with similar thermal blocking filters achieving attenuation at 45 dB when extrapolated to 80 GHz. Further evidence from quasiparticle lifetimes suggests  $<10$  aW. Additionally, radiation above 90 GHz will break Cooper pairs in the Al feedline and be absorbed there.

The microstrip design concentrates fields near the transmission lines, and the inter-KID spacing is  $\geq 200\times$  the silicon dielectric thickness and  $\geq 30\times$  the microstrip line width, leading to negligible physical coupling of fields between adjacent KIDs (estimated<sup>113</sup> to be  $-90$  dB). Based on this architecture, we choose not to randomize the RF frequencies, which would complicate characterization subject to tolerance variations and place dark channels in the atmosphere in proximity (in the readout) to bright channels, increasing susceptibility to Lorentzian crosstalk.

## 3.3 Spectrometer Package

The spectrometer package (shown in Fig. 13) comprises six smaller wedges attached by a larger frame into a hexagon  $\approx 15.5$  cm in the largest diameter,  $\approx 3.1$  kg, and registered using pins. The wedges can be closed into an optical test package for individual spectrometers. Each wafer fabricated has six spectrometers, which we release as separate dies and individually mount and characterize. Until process yield is well-characterized and controlled, we have opted to screen, select, and package spectrometers individually to achieve the best performance. Future focal planes may employ a single wafer with six spectrometers. Once characterized and accepted, individual spectrometer wedge packages combine into the focal plane without dismounting the spectrometers (wire bonds and mount clips remain in place). The enclosures of the flight spectrometer package and individual spectrometer test packages are blackened<sup>79</sup> (Sec. 2.1.3).



**Fig. 13** (a) The focal plane comprises six spectrometers that are held in segments and screened individually. The integrated package is  $\approx 15.5$  cm along its largest diameter. This view shows the kinematic mounting features and clips holding the wafers to the package. (b) View facing the focal plane showing package segments integrated into the focal plane, with a cutaway view showing the package lid's blackening features. (c) Section view of the focal plane with attached shrouding baffle, showing overall stray light control structures. The fastener below connects the package through a rod to the sub-K cooler.

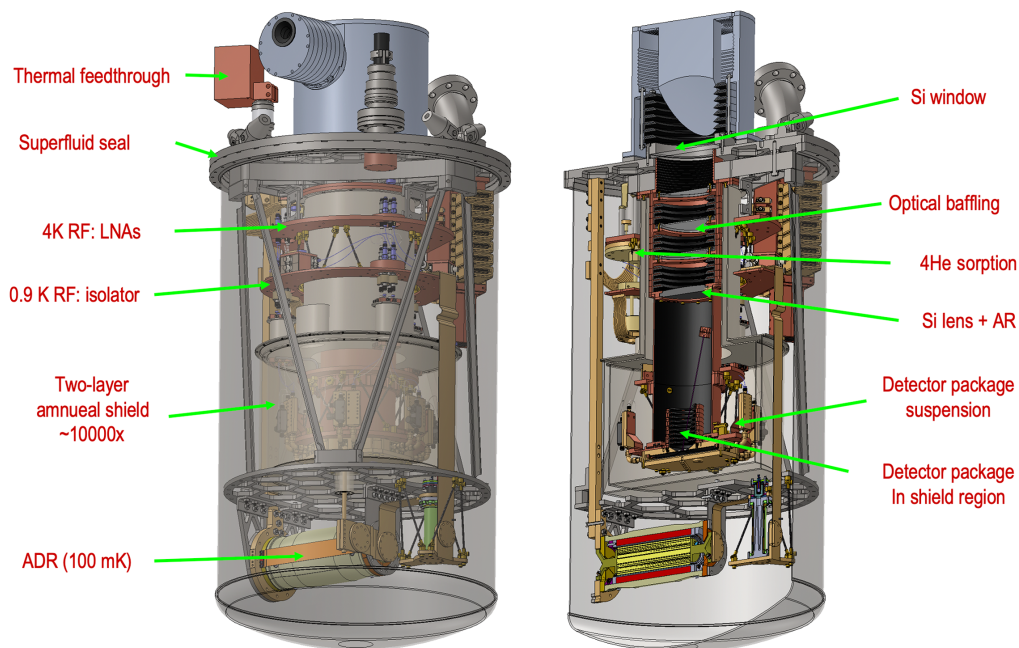


**Fig. 14** Overview of the EXCLAIM receiver.

A photoetched copper insert placed directly over the focal plane blocks light from impinging anywhere but on the lenslet in the six-spectrometer configuration.

A kinematic scheme fixes the spectrometer chips with a BeCu spring clip that pushes the spectrometer against both a pin in a groove (rotary freedom) and against a flat that locks the angle. Top clips press the spectrometer onto the package, which defines the optical plane. The mount positions of the spectrometers refer to the ambient temperature configuration and contract onto the target focal positions when cold. The packages are gold-plated copper (using non-magnetic flash) and use brass fasteners to avoid magnetic materials (Fig. 14).

### 3.4 Ambient Temperature Readout Electronics

EXCLAIM will use a readout based on the ZCU111 RFSoc FPGA, which can read up to four arrays with 2 GHz bandwidth using eight input and output channels.<sup>114</sup> The EXCLAIM implementation of the RFSoc will read two detector arrays in parallel, and capacity can be expanded to four arrays in future implementations. There are three intermediate frequency (IF) boards, each of which handles two spectrometers and follows TolTEC<sup>115</sup> board designs. Because of

significant overlap in the receiver design, Sec. 4.2 describes the cryogenic segment of the readout, and this section describes only the ambient-temperature electronics.

The ambient readout approach has balloon flight heritage from the Next Generation Balloon-borne Large Aperture Submillimeter Telescope (BLAST-TNG)<sup>116</sup> and the Far Infrared Observatory Mounted on a Pointed Balloon (OLIMPO).<sup>117</sup> These instruments use a ROACH2 architecture,<sup>101</sup> which employs a Virtex-6 FPGA per array with two input channels and two output channels and consumes 50-W per readout. This system provides the basis for readout software, procedures, and interfaces for the RFSoc. To give a fall-back, we keep the total resonator readout bandwidth within the 512-MHz range achievable by the ROACH2. Firmware based on BLAST-TNG is now implemented on the RFSoc and provides arbitrary waveform generation, polyphase filter bank (PFB), bin selection, complex multiply, vector accumulator, and data streaming functions. The measured readout phase noise in loopback (DAC to ADC) has a noise floor of  $-100$  dBc/Hz for 1000 tones. Ongoing firmware effort will extend the memory of the arbitrary waveform generator, enabling two parallel readout chains per RFSoc.

The RFSoc significantly reduces size, weight, and power requirements relative to the ROACH2. The power draw with active firmware on the RFSoc is 29 W, and each IF slice is 10 W, yielding 120 W for reading all six spectrometers. The RFSoc and IF slice each occupy one rack unit 44.45 mm (1 U), yielding 6 U for the complete readout. The readout will be enclosed to reduce interference with balloon-to-ground communications and will be verified preflight. For comparison, the older ROACH2 approach would require  $\approx 335$  W and  $\approx 14$  U volume.

The integrated system's gain response has an 8-dB slope across the band and will be corrected with equalizers. Antialiasing input filters follow a design similar to BLAST with  $<1$  dB reduction at the 490-MHz band edge. The IF and its carrier board work within the 3- to 4-GHz range of the detectors. The processing employs a Fourier transform with a length of 1024 (PFB with 1024 bins that have 500 kHz width), which is sufficient for reading 355 resonators over 490 MHz bandwidth and sampling the detector time constant. Amplifiers and variable attenuators condition the input and output levels to reach the desired read power and maximize ADC exercise from the input signal.

A Valon 5009 synthesizer provides the global clock and local oscillator across the readout channels and allows  $>10$  frequency steps across the  $-3$  dB point of the narrowest resonator. The buffer length for the output permits waveforms with 488 Hz tone resolution, significantly smaller than the resonators'  $Q$ -width of 194 kHz, under typical optical loading. The read tone frequency, amplitude, and phase per resonator are commandable to optimize performance. The electronics report output data at 488 Hz, sampling the optical point spread function through scanning (requiring  $>50$  Hz Nyquist). The relatively short flight presents no data storage challenge at a 488-Hz data rate (Sec. 5.3). In-band spurious tones are negligible for 355 detectors, following the performance on BLAST with  $>700$  tones. We measure spurious free dynamic range of 40 dB out of the DAC for 1000 tones.

## 4 Receiver: Mechanical, Thermal, and Electrical

### 4.1 Overview

The receiver is enclosed in a superfluid-tight shell<sup>76</sup> with a diameter that is constrained by the size of the flight-like LHe test system (Sec. 4.7). The overall height is limited by the dewar bottom when the receiver is in its flight optical configuration in the telescope (Fig. 4). The telescope provides a collimated optical input to the receiver, allowing significant flexibility in the baffling and shielding design. This versatility means that the telescope could also accommodate other receiver designs in the future.

In addition to the optics (Sec. 2.1.2) and spectrometer package (Sec. 3.3) described in the previous sections, the receiver contains (1) the magnetic shielding enclosure for the optics tube and focal plane, (2) the sub-K system to cool the focal plane to 100 mK, (3) the cryogenic segment of the spectrometer readout, (4) electrical interfaces to the ambient temperature electronics, and (5) thermal interfaces to the helium bath.

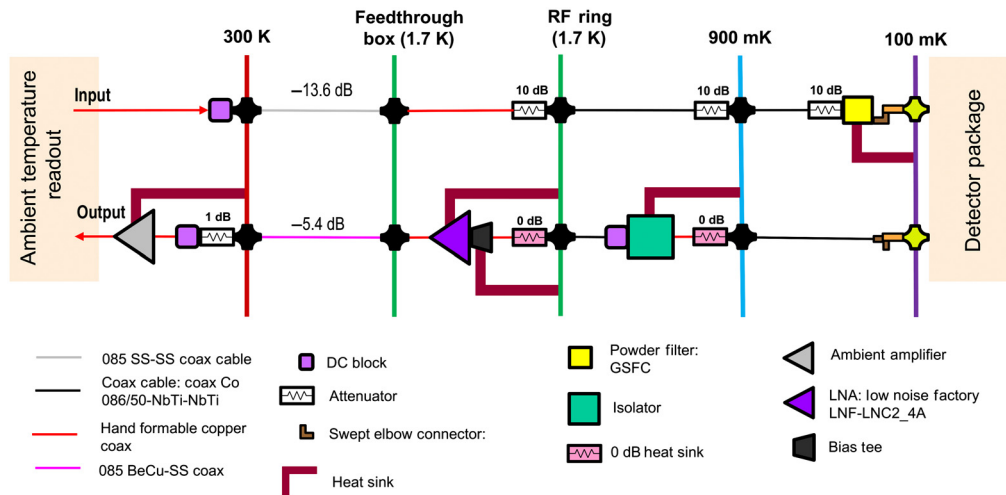


**Fig. 15** The cryogenic readout chain. The goals of the cryogenic readout chain are to (1) provide read tones at target power and high SNR to each resonator, (2) amplify the signal in the receiver to prevent loss of SNR to the ambient temperature readout electronics (Sec. 3.4), and (3) work within the limitations of the thermal system of the receiver and have a mechanical implementation there.

## 4.2 Cryogenic Readout Chain

Figure 15 describes the cryogenic components of the spectrometer readout chain. Two rings around the optics tube house the cryogenic RF components (Fig. 16). The upper ring acts as the bath plate for a helium adsorption cooler, which provides a 900-mK temperature stage. This ring houses six LNAs (Low Noise Factory LNC2\_4A<sup>118</sup>) and must handle their heat dissipation. The lower RF ring is a 900-mK thermal intercept of the coaxial cable lines going to 100 mK and is thermally suspended from the upper RF ring by a carbon fiber tube truss. Section 4.5 describes the thermal model of the integrated system. Isothermal connections use copper coaxial cables. Thermal breaks in the receiver use 2.19 mm NbTi coaxial cables. Section 4.4.1 describes considerations specific to the coaxial cable from the receiver to the ambient temperature electronics through the readout umbilical.

The LNA's baseline operation is at their highest bias, providing  $>32$  dB gain at  $\approx 1.6$  K noise temperature. The LNAs have relatively high return loss  $\sim 3$  dB, and we aim to remain above the

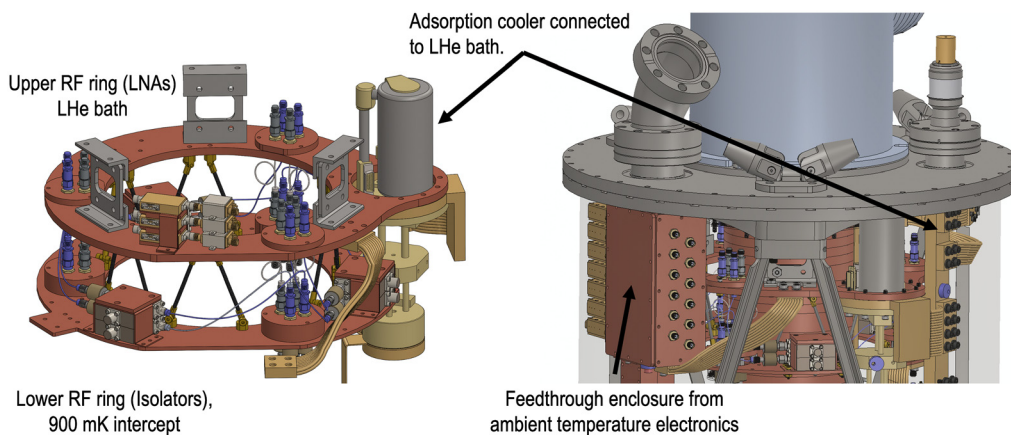


**Fig. 16** The receiver's thermal and electrical interfaces include (1) thermal feedthrough, (2) high-current feedthrough for vapor-cooled ADR lines (reverse side, not visible), (3) trunk bellows carrying detector readout and thermometry to ambient-temperature electronics, and (4) the optical window enclosed in a baffle assembly around the secondary mirror.

requirement of 12 dB return loss viewed from the resonators. A terminated circulator is used as an isolator between the resonators and LNA to reduce return loss to 16 dB. The system has low overall tone powers, and the LNA easily meets non-linearity requirements.

The highest expected read power is  $-95$  dBm, giving  $0.32$  pW per resonator, or  $0.673$  nW absorbed power in the 6 arrays. Assuming a conservative 20 dB in RF attenuation at 100 mK gives  $0.28$   $\mu$ W loading compared with  $1.32$   $\mu$ W from thermal conduction to the stage. In practice, optimal read powers at EXCLAIM's low optical backgrounds are expected to be  $\sim 1000\times$  lower, producing negligible load on the 100-mK stage.

### 4.3 Magnetic Shielding

The extended collimated optical region supports two layers of high-permeability shielding (Amuneal A4K<sup>119</sup>) with a  $\sim 3:1$  aspect ratio. An analysis using Ansys Maxwell<sup>120</sup> finds  $10^4$  axial and  $5 \times 10^3$  lateral suppression of fields at the focal plane. Axial fields are perpendicular to the spectrometer wafer, so they are the most significant concern. The shield has a removable lower segment that permits access to the focal plane assembly. We avoid additional superconducting shielding to limit pinned fields<sup>121</sup> and avoid nickel flash and magnetic components inside the shielded volume. Stray fields from the ADR (parallel to the coil, in mid-plane, 11 cm from bore) are estimated to be 3.35 G. There is currently limited information regarding the impact of magnetic fields on the performance of KIDs using an Al microstrip. The spectrometer test plan includes susceptibility measurements using a Helmholtz coil, and there are several approaches to improving the shielding, such as a superconducting Nb shield if needed.

### 4.4 Electrical and Thermal Interfaces

Figure 16 provides an overview of the receiver's electrical interfaces. Stainless steel bellows tubing carries the RF readout coaxial cable and DC wiring from the receiver to ambient electronics. It also acts as a vacuum pump-out port for the receiver and is accessible on the integrated gondola exterior. All interfaces on the receiver lid employ superfluid-tight metal seals. The bucket dewar system does not have a fixed-temperature intercept from ambient temperature to the LHe bath, so the readout umbilical to the receiver spans a 2-m run from ambient temperatures to the LHe stages in the receiver.

#### 4.4.1 RF segment

The spectrometer readout cryogenic chain (Sec. 4.2) has 12 total coaxial cable lines that run to the ambient temperature electronics. In signals outbound from the receiver, losses in the coaxial cable to the ambient temperature electronics increase the noise temperature through attenuation and thermal radiation in the warmer coaxial cable. Lowering RF attenuation requires increasing thermal loading in the receiver. Although the LHe bucket dewar can accommodate very high loads ( $\sim 1$  W), the receiver's capacity to manage thermal loading is limited to  $<180$  mW by the system of thermal buses that communicate heat from the inside of the receiver to the LHe bath. Therefore, the output chain requires choosing a suitable coaxial cable with low RF loss but tolerable thermal conduction.

For the six outbound RF coaxial cables, we baseline the use of 2.19 mm OD stainless steel coaxial cables with a beryllium copper centerline. We estimate thermal conduction and RF attenuation in the link to be 5.6 mW per output coaxial cable at 5.4 dB attenuation (220 K effective emission temperature), which gives a 30% increase in the effective LNA noise temperature at its highest gain. For the six coaxial cable inputs to the receiver, we use 2.19 mm OD stainless steel coaxial cable (shield and centerline). These have 2.4 mW thermal conduction per coaxial cable utilizing a model that agrees with recent measurement<sup>122</sup> and have 13.6 dB RF attenuation, which is acceptable in the input chain. The estimated thermal conduction through the RF coaxial cable link from ambient temperature interfaces to the LHe bath stage is 48 mW.

#### 4.4.2 DC segment

The housekeeping is allocated on six MDM37 connectors with 18 twisted pairs of 5 mil manganin, giving nine four-wire measurements per harness. This harness contributes 7.2 mW.<sup>123</sup> The LNA bias channels use 5 mil copper in the trunk for each of the six amplifiers (18 wires total, replacing manganin in a harness) to control Joule heating and yield an additional 22 mW loading from additional thermal conduction.

#### 4.4.3 High-current lines

Lines carrying current to the ADR must support  $\sim 10$  A and be normal metal because they run to ambient temperature. Conveying these through the bellows from ambient temperature to the receiver produces unmanageable thermal loading inside the receiver. We vapor cool<sup>76</sup> the high-current DC lines in the helium dewar space and pass these through a superfluid-tight high-current feedthrough (MPFPI a0757-1-cf, 8 conduits) to the receiver interior. In addition to supporting the ADR, this conduit carries lines for the adsorption refrigerator heater and its gas gap heat switch and the 100-mK gas gap heat switch. In addition to high-current lines, the ADR also has voltage taps to measure the drop across the superconducting coil in a four-wire configuration. These taps do not transmit any appreciable current and are implemented through the manganin harness in the vacuum bellows in two redundant pairs.

#### 4.4.4 Feedthrough assembly

A feedthrough structure in which the bellows enter the receiver (Fig. 16) serves to thermalize the RF and DC harnessing from the ambient-temperature electronics and block IR radiation that scatters down the bellows. The bellows do not allow a direct line of sight to 300 K, and reflections in the stainless steel tube suppress IR radiation. The feedthrough box takes several steps to control stray light into the larger receiver volume and sink the harnesses thermally: (1) its interior is blackened, (2) DC lines exit through powder filters,<sup>111</sup> and (3) the input and output coaxial cable lines are heat sunk. The feedthrough is also the vacuum pump-out port, and we implement a labyrinth with blackened walls that are relatively reflective to gas in a diffusive limit but absorb light.

The total thermal loading of the receiver interior from heat flow in the readout umbilical connection is 77 mW. In the thermal model, we add a significant margin (176 mW total) to account for uncertainty in the thermal conduction model.

### 4.5 Thermal Systems

#### 4.5.1 Thermal system design

The stainless steel shell of the receiver (Sec. 4.6) has poor thermal conduction. A commercial high-current vacuum feedthrough<sup>76</sup> brings a 0.75-in diameter high-purity copper rod through a superfluid-tight ceramic seal on a vacuum flange. A bus outside the receiver has a LHe reservoir supplied by superfluid pumps to ensure constant connection to the LHe bath. All critical thermal links in the receiver are gold-plated oxygen-free high-purity copper to achieve high conduction. For mechanically compliant connections to absorb tolerances and CTE, we use braided copper strap<sup>124</sup> and model the conduction using recent measurements<sup>125</sup> that include the effect of junctions.

The spectrometer requires temperature  $< 125$  mK (measured at the detector package) to ensure a negligible contribution (Sec. 3.2.3) from thermal quasiparticle generation. The sub-K system's threshold performance must permit  $> 4$  h of cold operation (one cryogenic cycle in flight) and baseline performance with 100 mK operation and  $> 12$  h hold. We also require that the sub-K system hold for  $> 8$  h to permit testing in a cryocooler test configuration with a bath stage up to 4 K. The ADR should also provide shielding to maintain magnetic fields  $< 5$  G at the position of the detectors so that fields are well-suppressed by the two-layer shielding for the Earth's field (Sec. 4.3).

Carbon fiber tube trusses suspend the cold stages. The lowest harmonic modes of the loaded 100 mK stage are modeled to be 60 Hz, above the highest signal frequencies  $\approx 30$  Hz. A re-entrant carbon fiber tube suspension with a 900 mK intermediate stage holds the spectrometer package. The 100- to 900-mK and 900 mK to bath suspension trusses are designed with the same angle and length, canceling the impact of thermal contraction. The stage suspensions are assembled on a jig to maintain the position of the focal plane relative to the optics. We have built a prototype of the carbon fiber tube suspensions and gluing jigs that validate the design. We have opted for carbon fiber for additional stiffness, dimensional control, and robustness to shipping vibration relative to Kevlar. If the carbon fiber tube fails in parachute shock or landing, catch screws will retain the package to displacements  $< 1$  mm to prevent damage. After flight-like testing at NASA-Goddard, the receiver remains integrated through shipping (Sec. 6.2). The catch feature implements a continuity test to determine if a suspension has failed after shipping.

Heated gas getters in the adsorption pump and gas-gap switches can produce stray radiation in the receiver cavity. Heat switch getter heaters will be wrapped in multilayer insulation (MLI) to control radiation. In 100-mK operation, the adsorption heater pump will be cold. In a single-shot configuration, the ADR gas gap will also be non-conducting (cold).

#### 4.5.2 Analysis of thermal conduction and heat capacity

The thermal system (Fig. 17) has well-defined nodes (which have high interior conduction) connected by links, so we solve for each node's equilibrium temperatures subject to the conductance of each link. Copper heat straps<sup>125</sup> define the high-conduction buses. The 100-mK stage is thermally isolated by (1) carbon fiber tubes (conductivity provided by the vendor<sup>126</sup>) for the RF ring and detector package, (2) NbTi<sup>127</sup> for coaxial cable lines, and (3) Kevlar<sup>128</sup> for the ADR salt pill. The other loading on the 100-mK stage originates from a re-entrant gas-gap heat switch,<sup>129</sup> which has off-state conduction of  $0.15 \mu\text{W}$  at this bath temperature. The heat switch allows the 100-mK stage to be coupled to the 900-mK stage for precooling to eliminate much of its heat capacity before launching to 100 mK.

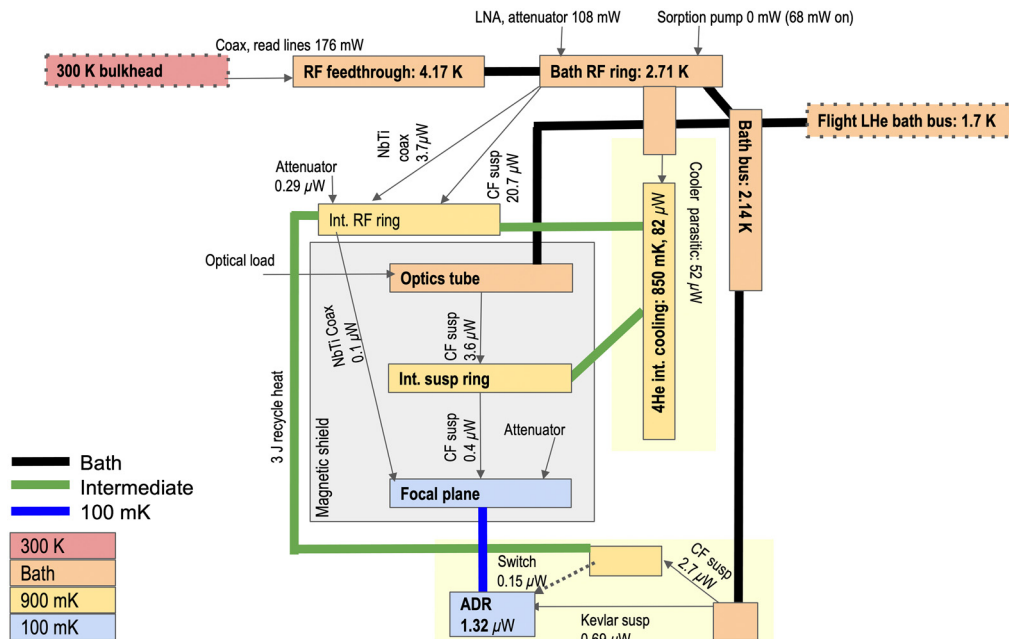


**Fig. 17** We calculate equilibrium temperatures and heat flows using a lumped thermal model. Values here are for the helium bath temperature at balloon float. Thick lines indicate high-conduction thermal buses, and thin lines are suspensions or low-conduction elements. Carbon fiber tube suspensions are designated by CF. The intermediate stage (int. above) with a  $^4\text{He}$  adsorption cooler provides significant margins by reducing the heat capacity and thermal loading of the ADR.

We assess the cooling energy or entropy required to cool the stages with both the adsorption cooler and ADR. For the adsorption cooler, we directly integrate the heat capacity to find the total energy. For the ADR, the salt cools in parallel with the stages, so the entropy provides the best assessment of the remaining cooling energy once the stage reaches the target temperature. We calculate specific heats for: (1) copper;<sup>130</sup> (2) blackening,<sup>79</sup> which is composed of SiO<sub>2</sub>,<sup>131,132</sup> EpoTek 377 (scaled from Stycast 1266<sup>133</sup> based on material measurements), and graphite;<sup>134</sup> (3) brass<sup>135</sup> for fasteners; (4) NbTi<sup>136</sup> for coaxial cable lines; (5) nickel<sup>137</sup> for magnetic material in the isolators; and (6) stainless steel<sup>138</sup> for RF hardware.

#### 4.5.3 Meeting sub-K cooling requirements

The adsorption cooler must have sufficient energy to cool the 900- and 100-mK stages and accept heat of magnetization from the ADR. From 1.7 K float conditions, we estimate that the LHe bath at the adsorption cooler and all lower stages launch from 2.7 K (with 1.7 K +  $\Delta T$  driven by the receiver bath stage conservatively handling 176 mW conducted through the read-out umbilical described in Sec. 4.4.4), requiring 1.4 J to cool to 850 mK. Additionally, the ADR is estimated to dissipate 3 J from the salt pill in cycling. From the 28-J cooling energy of the adsorption fridge,<sup>139</sup> we estimate 23.6 J remaining for cooling or 80 h hold time at 82  $\mu$ W loading.

A model of the ADR as a dilute CPA salt<sup>140</sup> agrees well with in-flight measurements of performance from Astro-H.<sup>110</sup> The ADR only needs to cool the 100-mK stage from  $\approx$ 900 mK, requiring 0.11 J/K cooling entropy and resulting in 308 mJ cooling energy. Total flight loading of the 100-mK stage is estimated to be 1.32  $\mu$ W, giving 65 h hold time with a considerable margin over mission requirements. In addition to the flight requirements from a pumped LHe bath, we also consider operation from unpumped LHe and a cryocooler for ground hold and testing configurations (Sec. 4.7). From a 4.4-K bath, parasitic loading increases to 7.3  $\mu$ W (10 h hold), allowing tests in unpumped LHe baths and cryocooler systems (improving further for 3 to 4 K cryocooler systems).

The adsorption cooler supports 100 mK operation because it cools most of the stage's heat capacity and provides an intercept for the mechanical suspensions and coaxial cables. This cooling provides a significant margin in flight operation and enables testing in unpumped and cryocooler systems. If the adsorption cooler fails, the ADR can support threshold (>4 h) operation in flight thermal conditions.

#### 4.6 Mechanical Design

The receiver window (Sec. 2.1) employs an indium seal<sup>141</sup> to remain superfluid tight, preventing LHe from entering the receiver volume, where superfluid films could spoil sub-K cooler operation. The receiver lid is lightweighted to control deflection at the window and increase its strength-to-weight ratio. An indium seal with 41.5-cm diameter closes out the receiver lid and shell. Interfaces to the receiver employ superfluid-tight metal seal flanges and welds.

An optics bench acts as the primary support structure within the receiver core. FEA analysis for the receiver lid, optics bench, ADR truss, optics tube, thermal suspensions, and magnetic shielding verifies that all pass CSBF flight mechanical loading requirements (Sec. 6.1). In addition to flight loading requirements, the receiver must also be robust to shipping vibration. All fasteners in the receiver will be staked (Henkel Loctite Hysol 9309.3 NA<sup>142</sup>), and counterbores and other features are modified to permit staking.

#### 4.7 Flight-Like Receiver Test Facilities

The integrated telescope and dewar cannot be tested on the ground in flight-like cryogenic conditions due to requirements for (1) a pressure dome across the 1.5-m diameter dewar and (2) a pump with sufficient throughput to simulate the upper atmosphere while also handling a high helium flow rate. Subject to this limitation, we test the receiver alone in flight-like conditions using a smaller LHe dewar (48.6-cm diameter and 152-cm depth) and transfer it to the telescope with no changes in configuration. The receiver's largest diameter is 44.45 cm, providing a space

for a LHe level gauge, superfluid pump conduits to the receiver's thermal interface, and harnessing. Flight-like testing will use a simulated telemetry link. To prepare for flight-like tests of the integrated receiver, receiver components will be tested in a cryocooler system, and the dilution refrigerator used for spectrometer characterization will be used to test flight software and electronics for the spectrometer readout.

The mounting of the receiver in the telescope allows it to be installed (Sec. 6.2) as an integral unit after flight-like testing (Sec. 4.7) and aligned to the telescope. The integrated gondola will also remain supplied with LHe during ground hold during the field campaign, allowing cryogenic tests of the integrated system with an unpumped LHe bath.

## 5 Flight Electronics and Software

In addition to the ambient temperature readout electronics (Sec. 3.4), there are electronics for switching and conditioning battery power; running survival heaters; and measuring currents, voltages, and ambient/cryogenic thermometry. This section describes these components and the flight computer and its software. These are based on the PIPER mission, which has shown nominal performance in these components in two engineering flights. Section 6.3 describes mechanisms and attitude control and determination system (ADCS) electronics.

### 5.1 Rack and Channel Allocation

Standard 19 inch racks house the instrument electronics. Rack units comprise the flight computer, high-current drivers, cryogenic housekeeping, ambient systems, and power control (all are 3 U). The electronics follow a PIPER design in which up to 20 boards draw power and communicate on a bus with one master board, which drives the overall clock for the electronics and packages data to send on a fiber optic to the flight computer. The cryogenic housekeeping rack unit has 5 PID controllers, 144 four-wire thermometers (12 boards), 64 ambient temperature channels (2 boards), and 32 analog input channels (1 board). The high-current drivers for the sub-K housekeeping segment support (1) the ADR, controlled by one PID board with  $\pm 12$  V FET driver, (2) 900 and 100 mK stage gas-gap heat switches controlled by analog output with a  $\pm 30$ -V Op-amp, and (3) the adsorption pump heater through analog output with  $\pm 30$  V Op-amp.

The ambient system rack unit has 20 boards that provide an interface to the telemetry, 32 fast readout channels for analog attitude sensors, 64 ambient temperature channels (2 boards), 64 analog outputs (2 boards), 224 analog inputs (7 boards), 2 servo motors (lid with spare, 2 boards), and 24 low-power survival heater channels with software control (4 boards). Within the analog output channels, there are 24 survival heaters, 16 LHe superfluid pumps, and two motors with three control channels (46 of 64 channels allocated). There are analog inputs for voltage and current monitors for each of the 48 power control channels, 24 survival heaters, 4 level sticks, 16 LHe pumps, 2 ion gauges (2 channels each), 2 lid limit switches and 1 tachometer, and 1 interface for ambient air pressure. This allocation uses 192 of 224 available channels.

### 5.2 Power

All electronics other than the ADR are powered by SAFT<sup>143</sup> 30 V lithium sulfur-dioxide primary cells with 30 A h capacity. Four Powersonic 12 V lead-acid batteries with 100 A h capacity power the ADR and attitude control motors. Lead-acid batteries are used in these systems because they can safely handle back-EMF from motors and high-current transients during a superconducting magnet quench. All batteries are contained in cases or behind structural elements to prevent damage in the landing. For ground operation, the gondola is powered by rolling power supply racks. Shifting to flight operation requires swapping the ground power for flight batteries in the input power umbilical. The power controller can be powered down except for one control channel to limit quiescent draw while on battery, especially in ground-hold during flight attempts.

Switched-mode DC-to-DC converters in a 2-U rack unit provide multiple voltages. The power controller has 48 switched high-power channels on 16 boards and one relay board with 12 channels with Consolidated Instrument Package (CIP)<sup>144</sup> discrete control (Fig. 18) for

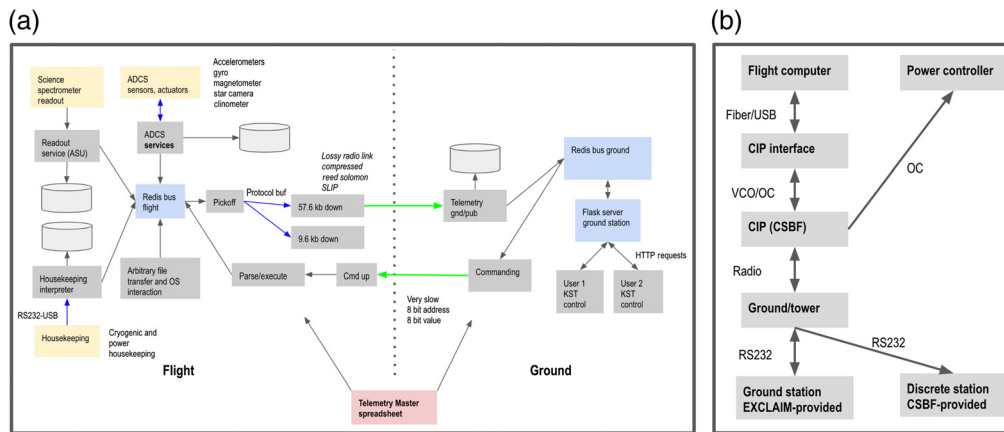


**Fig. 18** (a) Block diagram of the EXCLAIM software. Yellow boxes represent hardware that communicates with the flight computer. Each service is a single-threaded, asynchronous python process. The services communicate through a Redis database. (b) Hardware interfaces between the balloon telemetry and EXCLAIM systems. VCO refers to a voltage controlled-oscillator interface, and OC is an open collector interface.

systems requiring  $<0.5$  A. These 48 + 12 channels use 60 of the 77 available discrete commands. Each power card can control up to three channels.

### 5.3 Flight Software and Computing

The flight computer communicates with detector readout electronics, the star camera, and housekeeping electronics. The software comprises several single-threaded Python services that handle individual tasks and communicate over a redis database bus. The data rate from the detectors is 17 MB/s for 355 detectors ( $I$  and  $Q$ ) in 6 spectrometers at 488 Hz and can use a single 2 TB solid-state drive (30 h of detector data). Housekeeping and star camera data require an additional 1.5 and 36 GB, respectively, and will be saved on the same drive. The flight computer performs limited analysis of data in-flight. Star camera solutions can be requested (but are not part of the online pointing model, Sec. 6.3) and verified on the ground. Flight software determines resonator readout tone frequencies and powers (BLAST-TNG heritage).

The CIP provides telemetry to the gondola and has 77 open-collector discrete command channels for the power control relays, a 16-bit parallel command uplink to the flight computer, and two downlink channels (9600 and 57,600 baud) for data to the ground. (Figure 18 shows the physical interfaces.) The CIP provides over-the-horizon and line-of-sight antennas, and a fiber-glass mast supports a global positioning system (GPS) antenna. Unlike the Antarctic program's telemetry package, the conventional CIP does not provide additional satellite links. In flight-like testing and ground operation, the software works interchangeably between the CIP and a serial fiber-optic interface that simulates the CIP telemetry.

Telemetry consists of regular stream reporting and specialized data requests, transmitted in parallel through the 9600 and 57,600 baud links. Science operation must be possible using the 9600 baud link as a fallback to the 57,600 baud link. The regular stream reporting allocation utilizes 7600 baud of uncompressed data, leaving a margin to send data requests. The uplink provides one byte each for command address and value, and a master telemetry spreadsheet defines packets and handling of the uplink commands.

## 6 Gondola Systems

### 6.1 Mission Mass, Power, and Balloon Requirements

EXCLAIM can fly on either the 11 million-cubic-foot (MCF) or 34 MCF heavy balloon class, reaching an altitude range of 27.5 to 37 km and capped at 3400 kg. The specific altitude depends

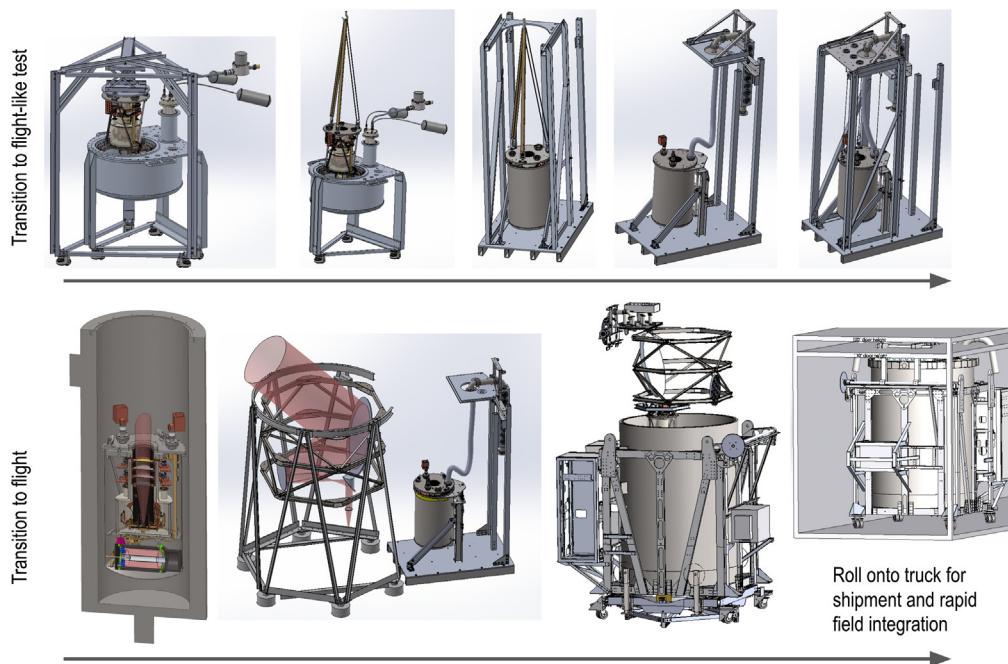
on the weather conditions. The flight must achieve a minimum altitude for the LHe to reach its superfluid transition, allowing fountain-effect pump operation (26.5 km and  $\approx 10$  Torr) and a margin for variations, giving a  $>27.5$ -km requirement on altitude. Weather conditions also set a minimum altitude, typically  $>29$  km and specific to the launch day. The gondola provided by the science team has an estimated mass of 2400 kg (science mass). In the field, the gondola houses the CIP telemetry hardware and yields 2480 kg (dry mass). Adding cryogenics (310 kg) and ballast (350 kg) yields 3140 kg before flight. We apply a mass growth allowance to model changes in mass through the mission cycle based on component maturity, which yields 3340 kg.

The gondola frame has four brackets at its base that can be used either for casters (ground), jack stands (flight preparation), or crush pads (flight). A rotator pin connects the gondola rigging to the flight train (Sec. 6.3). All gondola structures meet the load analysis and envelope requirements [Structural Requirements and Recommendations for Balloon Gondola Design (820-PG-8700.0.1), LDB Support for Science EL-100-10-H Rev. B]. We additionally apply these tests to the telescope and receiver.

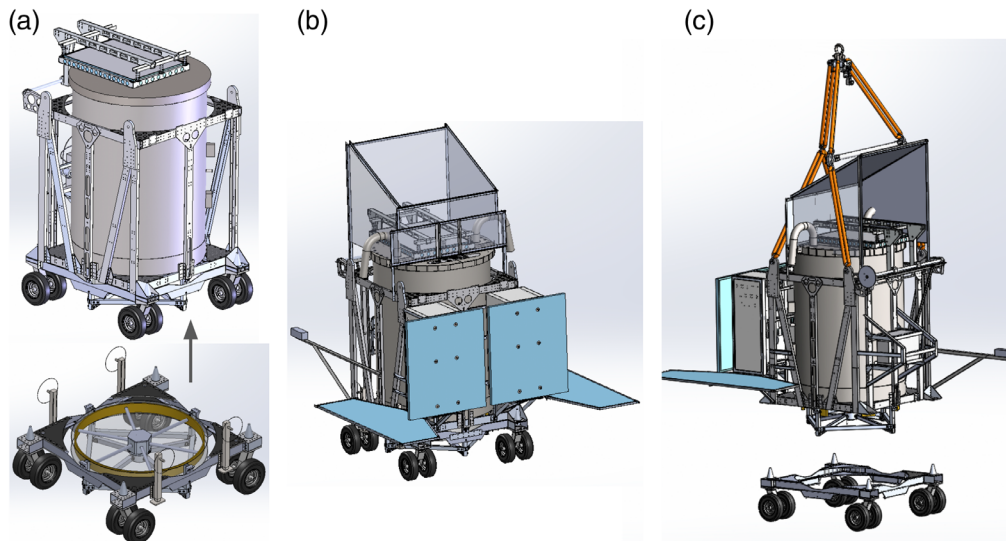
## 6.2 Integration and Transportation

Figure 19 describes the receiver's integration from a long-term cryocooler test system to a flight-like test to integration with the telescope and gondola. A standard 120 inch truck bay height is sufficient for shipping the gondola on small transport casters. This shipping allows the integrated instrument to be delivered to the flight location and avoids complex integration and testing of the receiver in the field, but it also requires that fasteners and staking withstand shipping vibration. The catch/continuity test (Sec. 4.6) can verify the receiver's 100 mK suspension after shipping. The truck must be refrigerated and monitored to remain  $<35^\circ\text{C}$ , due to the thermal sensitivity of hydrated ADR salts.

Figure 20 depicts the integration sequence to prepare the dewar segment of the gondola for flight. After arriving in the field, the gondola dewar is lowered onto a field operation cart, which also maintains the reaction wheel assembly. The reaction wheel assembly is mounted to the



**Fig. 19** Integration of the receiver into the telescope and gondola. Upper left: the receiver core is tested in a long-term test cryocooler system. Once the performance is verified, it is lowered into the flight-like pumped LHe test dewar. In parallel, the telescope is assembled on a stand. After flight-like tests pass, the receiver is integrated with the telescope, and the assembly is lowered into the dewar. This assembly is shipped in a standard freight truck to the launch facility.



**Fig. 20** Integration of the EXCLAIM gondola. (a) The gondola dewar segment is lowered onto a field cart that facilitates flight operations. Alignment cones guide the gondola onto the stand. The reaction wheel system is initially integrated with the field cart. (b) The reaction wheel is decoupled from the field cart and raised with jacks to connect to the bottom of the dewar. Electronics and thermal control interfaces are then installed. (c) Rigging is attached, and the gondola flight assembly is lifted off the field cart. A ballast hopper and crush pads are then attached to the bottom of the gondola assembly.

gondola dewar in this configuration, allowing the integrated flight assembly to be removed from the field cart.

### 6.3 Attitude Determination and Control Systems

EXCLAIM uses a sinusoidal azimuthal scan to survey (Sec. 1.3.2) rising and setting fields at a fixed elevation. A reaction wheel executes the azimuth scan and is a large rolled brass hoop in a spoked-wheel configuration (shown in Fig. 20). The wheel has a moment of inertia of  $30 \text{ kg m}^2$  (total mass  $75.8 \text{ kg}$ ) relative to the overall gondola azimuth moment of inertia of  $2665 \text{ kg m}^2$ . Momentum is dumped to the balloon to maintain the reaction wheel motor speed below its saturation due to back EMF.<sup>145</sup>

The peak torque and angular rate to execute the scan are  $27 \text{ N m}$  and  $161 \text{ deg/s}$  on the reaction wheel and require  $29 \text{ W RMS}$  power (assuming 80% efficiency). A Kollmorgen D081 brushless direct-drive DC motor drives the reaction wheel. This motor can achieve a peak torque of  $45.0 \text{ N m}$ , which offers a 40% margin over the peak torque required to execute the scan. The direct drive simplifies design and operation, eliminates backlash, and reduces vibration. The rotator follows PIPER heritage and acts as a momentum dump to desaturate the reaction wheel rather than directly helping the reaction wheel with the scan.

Pointing design and requirements apply to online (executing the target survey) and offline (producing maps) operations. Offline pointing must have noise  $<2\%$  (5 arc sec) of the optical FWHM to control jitter's impact on the effective angular resolution. Offline pointing will be based primarily on star camera measurements acquired at the scan turnarounds and tied together by gyroscope data, using a clinometer to establish tilts. Section 7.3 describes source observations to calibrate fixed offsets of the telescope boresight and sensors in the offline pointing model.

Online pointing must be sufficient for establishing the field center ( $<1 \text{ deg}$ ) and controlling the scan speed and total throw to maintain target fields. Online pointing through a Kalman filter and control system uses gyroscope and magnetometer sensors for velocity and position, respectively. Because of the more lax absolute pointing requirements, online pointing will not require a real-time star camera, simplifying computing and improving robustness. The magnetometer

can have offsets due to stray fields in flight or during calibration. We will use dedicated stare mode pointings early in the flight to calibrate an offset between the magnetometer heading and azimuth determined by the star camera and Sun sensor. Additionally, as part of a staring mode before starting a survey scan, the star camera validates the field center. The magnetometer can be used to determine pointing to  $\sim 1$  deg sufficient for maintaining the target scan in parallel with signals from the gyro.

The star camera uses an imaging sensor (IDS UI-5480CP-M-GL) coupled to a 200-mm telephoto lens with a USB-controlled focus mechanism and achieves 2.27 arc sec resolution. It will acquire images in either stare mode or at scan turnarounds. For a typical  $3\sigma$  determination of centroids to one-tenth the pixel size, the star camera yields a 0.1-arc sec determination of the pointing ( $2\sigma$ ). A 3-axis fiber-optic KVH DSP-1760 gyroscope with angle random walk  $< 0.012$  deg/ $\sqrt{h}$  provides angular velocity information to tie the pointing between star camera determinations. The gyroscope will be magnetically shielded following an approach from BLAST<sup>146</sup> to manage susceptibility to fields. We will also fly a MEMS STMicroelectronics LPY403AL gyroscope for redundancy. For star camera acquisitions at the scan turnarounds, the gyro integrates errors between these position determinations, separated by 3.5 s. This cadence yields a drift of 2.33 arc sec ( $1\sigma$ ), assuming integrated errors in the three axes. In quadrature, the combined gyro and star camera give  $1\sigma$  errors of 2.24 arc sec, which is  $< 5$  arc sec or 2% of the most stringent FWHM at 540 GHz. The sensor platform and offline pointing are similar to SPIDER and BLAST.<sup>146</sup>

A SolarMEMS Technologies nanoSSOC-A60 determines the Sun's position to 0.5 deg in  $\pm 60$  deg about the aft direction for daytime pointing (which will be antisolar along the optical boresight). One TE Connectivity G-NSDPG2-005 digital clinometer measures tilt around the pitch and roll axes to 0.001 deg resolution. For redundancy, two additional AccuStar 02115002-000 analog clinometers will measure tilt around the pitch and roll axes to 0.05 deg resolution. A Jackson Labs Mini-JLT GPS-conditioned and stabilized oscillator provide timing (tying ADCS and detector systems), heading, and altitude information. We will fly redundant magnetometers (Honeywell HMC2004 and HMR2300) to determine the heading for online pointing. We synchronize ADCS and detector data following the approach of BLAST-TNG.<sup>145</sup>

We have performed a modal analysis of the flight train that describes swinging of the roll and pitch of the payload (22 s), counter swinging of the balloon and flight train (8 s), and swinging of the gondola relative to the flight train (1 s). These values are consistent with reported measurements.<sup>147,148</sup> The Medium-Scale Anisotropy Measurement Mission-2<sup>148</sup> found that these modes are excited by 10 arc min during ascent or slew to a source and damped on scales of 10 min.

## 6.4 Gondola Thermal

The gondola thermal design must account for ascent (rapid cooling), daytime float (solar direct and albedo loading), and nighttime float (radiative cooling and Earth IR loading). Electronics and batteries must be maintained between  $-20^\circ\text{C}$  and  $+40^\circ\text{C}$ . Figure 21 shows major thermal control features. We model each system component as isothermal nodes connected by conductive and radiative links. Additionally, we allow the extended radiators to have a gradient. Each node has an associated heater. All required view factors have been calculated with analytical formulas whenever possible; alternatively, physics-based estimates were used. Major electronics components are the flight controller, high-current controllers, power conditioning, and detector readout. The radiators have white paint that has solar absorptivity  $\alpha = 0.15$  and IR emissivity  $\varepsilon = 0.9$ . The sunshields and Earth-IR shields are foam panels covered with MLI blankets. Additional MLI protection is added to the bottom surfaces of the payload to decrease the effects of the albedo and Earth-IR.

Thermal simulations bracket a hot and cold case for operations. In the hot case, we take a solar constant equal to  $1419$  W/m<sup>2</sup>, Earth blackbody temperature 285 K (emissivity 1), atmospheric blackbody 230 K (emissivity 0.1), and ground albedo 0.032. In the cold case, we take a solar constant  $1317$  W/m<sup>2</sup>, Earth blackbody temperature 250 K (emissivity 1), atmospheric blackbody 220 K (emissivity 0.01), and ground albedo 0.028. In addition, we look at dawn and noontime conditions to evaluate different solar loads, namely a solar elevation angle  $\beta = 0$  deg

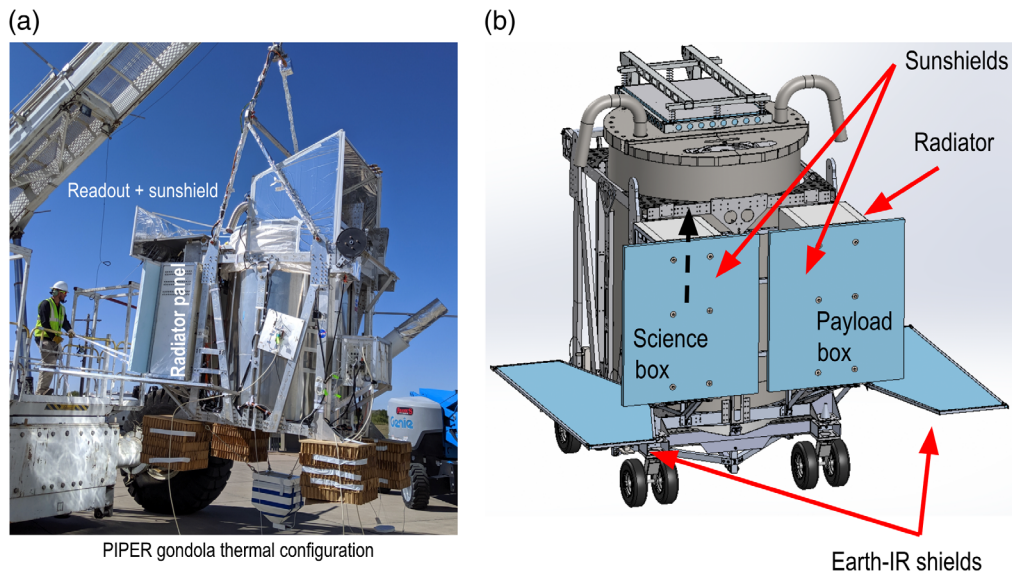


**Fig. 21** (a) PIPER heritage gondola showing major thermal control components. (b) EXCLAIM gondola showing Earth-IR shields and radiators behind sunshields.

corresponding to dawn and  $45 \text{ deg} \leq \beta \leq 79 \text{ deg}$  corresponding to local noontime between May and October. With conservative estimates of the payload power use, temperatures are maintained within operating range and require heaters in ascent and nighttime float.

## 6.5 Operation

The dewar lid has several features that support cryogenic operation. The process for cooling the telescope first uses liquid nitrogen to remove most ambient-temperature heat capacity. The liquid nitrogen is boiled off, and liquid helium transfer proceeds until the receiver is submerged. Passive boiloff gas must be allowed to escape the dewar while keeping the ambient atmospheric gas out. We employ a gas trap (elbows on the top of the gondola in Fig. 21), which operates as an inverse drain trap where the elbow holds less dense helium exit gas. The receiver bellows containing the readout coaxial cable, and the housekeeping harness exits the cryogenic space through a dewar bulkhead. Additional instrumentation in the cryogen space (thermometry, LHe level-measurement sticks, receiver high-current channels) exits the lid in insulated assemblies. The overall lid is foam surrounded by a riveted stainless steel sheet shell, closed against an O-ring to maintain gas tightness. A shroud of enclosed fiberglass insulation below the lid insulates the upper section of the dewar.

While waiting for a flight opportunity, the dewar lid hatch must remain closed to maintain a dry helium atmosphere in the telescope. The hatch seals against the lid with Buna-N rubber foam. PIPER observed  $10.5 \pm 1.6 \text{ l/h}$  passive loss on the ground. Several continuous liquid helium level sticks (American Magnetics, 36 inch LHe level stick for superfluid operation) and a custom backup level-measurement stick of discrete, thermally isolated thermometers with heaters monitor the helium level. The overall system requires three days to cool and four days to warm through a process that flushes dry gas to avoid condensation.

There are two phases of cryogenic operation in flight. First, in the ascent and flight hold phase, the dewar hatch remains closed to limit cryogen boiloff and maintain the telescope in a dry helium environment. Then when the science operation is ready to begin at float altitude, the dewar hatch opens. Based on its dimensions, EXCLAIM is expected to have active loss rates similar to PIPER, which lost  $100 \pm 12 \text{ l/h}$  (giving  $7 \text{ m}^3/\text{s}$  gas evolution in float conditions). At the temperatures inside the dewar, gaseous helium is denser than the surrounding air and forms a cushion of outflowing gas, observed in PIPER and ARCADE.<sup>51,52</sup> We will additionally employ a laser reflectometer near the primary mirror to monitor for condensation. In science operation,

the receiver window must be below the liquid level, yielding 1360 l of storage or  $\approx 12$  h of cryogenic operation (assuming some residual volume in the dewar will be inaccessible to the pumps). We plan for 200 l of reserve (1560 total liters) near the start of the science operation, and a high-power heater can quickly burn off the extra liquid to bring the helium level to the top of the receiver. A morning launch from Ft. Sumner, New Mexico, must additionally allocate for passive helium loss, measured at 6.4 l/h (PIPER) during a daytime hold. In ascent, PIPER finds that 35% by volume (27% by mass) of the original fill boils away, so an afternoon (Palestine, Texas) launch requires a 2400-l fill, and a morning (Ft. Sumner, New Mexico) launch requires 2479 l (assuming that the hatch remains closed until late afternoon). The launch mass budget includes liquid helium at 125 g/l.

A hanging assembly below the telescope frame maintains a bracket with superfluid pumps and a large boiloff heater in the bottom of the dewar.<sup>53</sup> Preliminary superfluid pump assignments are (for 16 in total): (1) four for the primary mirror, (2) two for fold mirror, (3) four for dewar lid regions near the optical exit aperture, (4) two redundant pumps for the receiver bath bus, (5) two redundant for secondary mirror and fore-baffle structure, and (6) two redundant for high-current feedthroughs. After the science operation, the boiloff heater purges the remaining cryogens, and the dewar hatch is closed for the descent. After recovery, the heater boils off any remaining cryogens.

## 7 Science Operation

### 7.1 Forecast Methodology

We model the cosmological signal as having both gravitational clustering<sup>149</sup> and correlated shot noise.<sup>19</sup> The sensitivity model uses Gaussian errors for the two-point cross correlation of EXCLAIM and BOSS, and the errors incorporate both spectral and spatial resolution effects.<sup>33,36,150</sup> This approach is numerically simple for parameter exploration and agrees with the simulated analysis of angular cross correlations between redshift slices,  $C_\ell(z, z')$ .<sup>151</sup> Forecasts use a Gaussian convolution to model the spectral resolution, where the Gaussian width is the second moment of the spectrometer's spectral response. In practice, the main lobe of the  $\sin^2$  response is  $\approx 4\times$  more compact than its second moment, allowing additional sensitivity to the cosmological signal. Calculations here use the more conservative spectral resolution and will be updated based on spectrometer characterization.

We include BOSS survey noise through an effective galaxy density  $\bar{n}$  for the MAIN,<sup>152</sup> LOWZ,<sup>153</sup> CMASS,<sup>154</sup> and QSO<sup>155</sup> galaxy redshift samples. An upcoming publication will describe the forecast and science goals. Here we consider constraints on the isotropic power spectrum at all scales, and later work will develop information from the range of spatial scales and redshift space distortions.

KIDs are known to have noise with  $1/f$  character from intrinsic device effects and readout noise.<sup>106,156</sup> One approach to the requirements is to specify the knee-frequency and white noise levels of the detectors. These requirements are coupled, and further, the acoustic noise of the KIDs may not follow a single  $1/f$  spectral performance (if there are multiple noise sources or intrinsically non- $1/f$  contributions). We instead develop a weighted NEP as a function of acoustic frequency  $f$  to form an effective NEP. This NEP is the equivalent white noise level that would give the same science constraint, and it depends on how the  $1/f$  in the time domain turns into map noise and how map noise on different scales impacts the final science.

We translate a given acoustic frequency in the detector time-ordered data into spatial modes using an approach from analogous raster-scanning CMB experiments.<sup>157</sup> The final science cross correlation uses information from all spatial scales in the survey, but the contribution to sensitivity is strongly scale-dependent. At large spatial scales, there are relatively few independent Fourier modes that contribute. Conversely, toward smaller spatial scales, the instrument's angular resolution reduces the information content. Simulations determine the contribution  $W(f)$  of time-ordered data at acoustic frequency  $f$  to the final science sensitivity. Figure 22 shows  $W(f)$  for the scan strategy. The effective NEP of the KID labeled with index  $i$  and weighted over this science band is

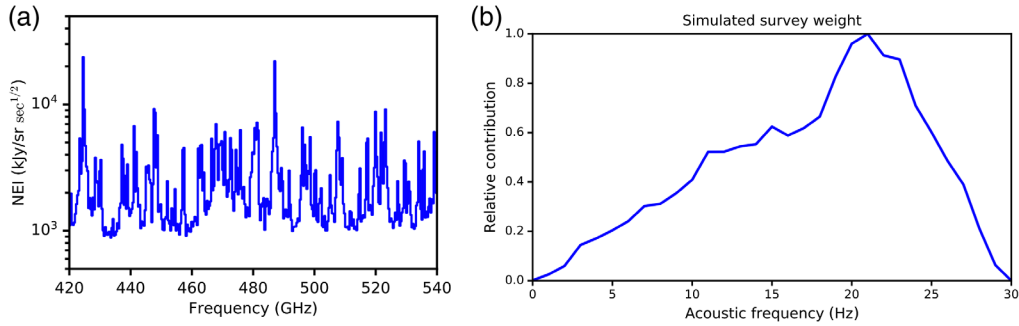


**Fig. 22** (a) NEI of the integrated instrument. This combines the optical loading and efficiency model with the spectrometer and detector design models. (b) Acoustic frequency weight derived from simulations of the scan strategy, with information content peaking from  $\sim 20$  Hz in the time-ordered data.

$$\widehat{\text{NEP}}_i = \left( \frac{\sum_j W(f_j) \text{NEP}_i(f_j)^{-2}}{\sum_j W(f_j)} \right)^{-1/2}, \quad (3)$$

where the sum runs on acoustic frequencies  $f_j$  indexed by  $j$ . This has the form of an inverse-variance weighted noise.

The spectrometer comprises  $N_{\text{det}}$  KIDs in its focal plane, each of which are subject to different loadings from the upper atmosphere (described in the loading model, Sec. 2.3) and so have a range of noise performance (Fig. 22). The effective NEP of the spectrometer, which accounts for variations in NEP per KID channel, is

$$\overline{\text{NEP}} = \left( \frac{\sum_{i=1}^{N_{\text{det}}} \widehat{\text{NEP}}_i^{-2}}{N_{\text{det}}} \right)^{-1/2}, \quad (4)$$

where  $\widehat{\text{NEP}}_i$  is the acoustic band-averaged NEP of KID with index  $i$ . This form can account for yield by treating a dead detector as having an infinitely large NEP. For example, if all detectors have the same NEP, but  $N_{\text{live}}$  detectors are live, then the effective NEP is penalized by a factor  $\sim \sqrt{N_{\text{det}}/N_{\text{live}}}$ .

In addition to the detector system, the atmosphere may also contribute to the  $1/f$  noise characteristics observed in flight. All detectors in one spectrometer see the same atmospheric column. The six detectors will also have near-field beams that substantially overlap through the nearby atmosphere. Photon noise is strongly in the shot-noise regime, so photon arrivals and their white noise NEP contribution are uncorrelated across detectors. At this time, the power spectrum of atmospheric fluctuations in the EXCLAIM band at balloon float altitude is not sufficiently well-described to predict the  $1/f$  noise level. Because all spectrometer channels look through the same column, the atmospheric contribution to  $1/f$  will appear as a rank 1 common mode. Similarly, drifts in detector stage temperature will appear as common mode (rank 1). However, thermally generated quasiparticles are exponentially suppressed at 100 mK operation (Sec. 3.2.3), well below  $T_c = 1.33$  K. The cosmological signal is nearly full rank, so residual atmospheric removal should not strongly impact the signal, except at large spatial scales. Most of the cosmological information is contained in shorter spatial scales, where there are numerous modes. The mission sensitivity builds in a significant margin (Sec. 7.2), and these correlated  $1/f$  and cosmic ray effects will be characterized after the first engineering flight.

Previously published forecasts<sup>158,159</sup> assumed a blanket factor of three deviations from background-limited performance and 30% spectrometer efficiency. Here we update these forecasts for the CBE design and allocate margins below. In addition to a detector noise model, the CBE also updates previous results by moving from 3.6 arc min FWHM (early beam model) to the model (4.25 arc min at 470 GHz) described in Sec. 2.2, moving cold stop spill efficiency to the spectrometer efficiency, and updating telescope efficiency. With these updates, we find expected  $2\sigma$  sensitivity to the surface brightness-bias product for  $0 < z < 0.2$  (SDSS MAIN) for CO  $J = 4 - 3$ ,  $J = 5 - 4$ ,  $0.2 < z < 0.4$  for  $J = 5 - 4$ ,  $J = 6 - 5$  (BOSS LOWZ),  $0.4 < z < 0.7$

for  $J = 6 - 5$  (CMASS), and  $2.5 < z < 3.5$  for [CII] (QSO) are  $\{0.08, 0.14, 0.17, 0.2, 0.26, 7.2\}$  kJy/sr, respectively. Figure 1 of the science introduction shows how these measurements constrain the current space of models.

Analysis of the mission data will follow approaches developed for single-dish intensity mapping for 21 cm emission with the Green Bank Telescope.<sup>10,46</sup> This extends mapmaking algorithms developed for CMB data analysis to multiple frequency slices. Following the formation of the data cube of maps, the data will be analyzed using an optimal quadratic estimator approach to estimate the cross-power variance. Additionally, we have developed a new spherical harmonic tomography method (following application to galaxy redshift surveys<sup>160-162</sup>) that retains a likelihood in the data cube space through the cross-power anisotropy between frequency  $\nu$  and redshift survey slice  $z$ ,  $C_\ell(\nu, z)$ . Both the optimal quadratic estimator and the tomographic method include foreground and data variance deweighting through their covariance. A forthcoming publication describes mission forecasts including foregrounds, which are lower than in the 21-cm regime. Bright atmospheric lines are analogous to the deweighting of radio-frequency interference in the 21-cm analysis. Mode counting for sensitivity estimates here includes the effective weighting of this bright forest of lines. Overall, the large margins to threshold science requirements can absorb data quality masking, filtering, common mode removal, and other effects that are difficult to anticipate before flight data are acquired.

### 7.2 Sensitivity and Allocation of Margins

The design and performance described throughout are for CBEs. Based on the instrument model developed in previous sections, we can identify key performance parameters and margins for deviation from CBEs to remain within threshold science (Fig. 23). Threshold science is defined

Parameter name	System	Current best estimate	Units	Maximum (worst) expected value (hardware)	Maximum (worst) possible value (science)	NEP under MPV (instrument), impact in quadrature	NEI under MPV (science), impact as product.
Telescope efficiency	Optics	0.876	Fraction	0.800	0.740	0.9	N/A
Spectrometer efficiency	Spectrometer	0.23	Fraction	0.13	0.07	1.8	N/A
Excess NEP	Spectrometer	1.00	Fraction	N/A	2.6	2.6	N/A
Spectral resolving power	Spectrometer	512	Unitless	438	364	1.1	0.89
Stray power: in-band diffraction reflected (ghosts)	Spectrometer	-38	dB	-32	-30	1.9	N/A
Stray power: in-band optical chain thermal emission (diffraction)	Optics spectrometer	0.10	FW	0.20	0.40	1.5	N/A
Altitude	Survey	36	km	33	29	2.3	N/A
Detector/spectrometer yield	Spectrometer	0.97	Fraction	0.67	0.30	N/A	0.56
Cosmic ray deadtime	Spectrometer	0.003	Fraction	0.030	0.050	N/A	0.97
Effective angular FWHM	ADCS	4.3	Arcmin	5.0	7.0	N/A	0.75
Integration time	Survey	8	Hours	8	6	N/A	0.87
<b>Multiplier</b>						4.2	0.31

Derived instrument sensitivity	NEP @ stop	NEP @ detectors	Instrument NEI
CBE NEP	1.7E-18	3.9E-19 W/rtHz	1.5E+03 kJy/sr rtsec
MPV NEP, all terms	7.1E-18	4.9E-19 W/rtHz	7.6E+03 kJy/sr rtsec

Derived science requirement	
CBE NEI	2.5E+04 kJy/sr rtsec
MPV NEI	7.6E+03 kJy/sr rtsec

**Fig. 23** Key performance parameters and their allocation of margins. Based on the instrument model, we can assess the sensitivity of intensity mapping science to possible departures from the CBEs. Some departures from CBEs impact both the threshold sensitivity requirement from science ( $NEI_{sci}$ ) and the sensitivity of the instrument ( $NEI_{inst}$ , implemented in the NEP column). For example, decreases in spectral resolution decrease sensitivity to the line intensity mapping signal (through thicker spatial slices with less density contrast) and increase instrument noise (through mixing bright atmospheric lines into dark atmospheric windows). Although yield and cosmic ray deadtime could be incorporated in the effective NEP, they are implemented as a decrease in the effective integration time and so decrease the required NEI. The maximum expected value refers to the largest expected deviation of a performance parameter based on the design analysis and prototype work. The maximum possible value (MPV) is the deviation of a performance parameter that will allow threshold science. There is a total margin of 14 $\times$  between the CBE performance and threshold science (described in the text). The total margin is allocated as MPV across all of the performance parameters.

by (1) reaching  $>4\sigma$  sensitivity to CII intensity from  $2.5 < z < 3.5$  at a surface brightness from initial cross-correlation measurements<sup>14</sup> with BOSS quasars and (2) constraining the evolution of cold gas through a  $>3\sigma$  measurement of CO  $J = 4 - 3$  emission  $0 < z < 0.1$  and CO  $J = 6 - 5$  transition from  $0.28 < z < 0.64$ , under the assumptions of model A of Ref. 35 and in cross correlation with BOSS galaxy redshift survey data. The first goal refines the preliminary indication<sup>14</sup> of CII measured in BOSS quasars  $\times$  Planck 545 GHz. We find a factor of  $14\times$  between the CBE and threshold science instrument sensitivity requirements. The margin between CBE and threshold can be allocated across several instrument parameters. The high overall margin means that each performance parameter can be allocated significant margins in performance while still advancing the state-of-the-art in intensity mapping.

The instrument performance can be summarized by its noise-equivalent intensity ( $NEI_{\text{inst}}$ ) on the sky and must meet the required sensitivity for science ( $NEI_{\text{sci}}$ ), giving

$$NEI_{\text{inst}} = (NEP/\sqrt{2}) \frac{dI}{dP} < NEI_{\text{sci}}, \quad (5)$$

where NEP is the array-effective noise equivalent power. Here power  $P$  is defined at the input to the spectrometer, and intensity  $I$  is surface brightness on the sky. We evaluate the impact of the key performance parameters on these terms using simulations or analytic estimates. Telescope efficiency reduces the responsivity  $dP/dI \propto \eta_{\text{tele}}/\eta_{\text{tele}}^{\text{CBE}}$ , but it also reduces photon loading, giving  $NEP \propto (\eta_{\text{tele}}/\eta_{\text{tele}}^{\text{CBE}})^{1/2}$  (in the background limit). Spectrometer efficiency results in  $NEP \propto (\eta_{\text{spec}}/\eta_{\text{spec}}^{\text{CBE}})^{-1/2}$ . The difference in NEP scaling relative to telescope efficiency is due to the fact that power in NEP is defined at the stop before the spectrometer but after passing through the telescope.

The spectral resolving power impacts the NEP as  $NEP \propto 0.044 \exp(-3.2(R/R^{\text{CBE}} - 1)) + 0.966$  and impacts the required  $NEI \propto (R/R^{\text{CBE}})^{0.35}$ . For the limit of high  $R$ , the NEP only improves by 3% because the CBE resolving power  $R = 512$  has sufficiently resolved the atmospheric lines at the nominal altitude. Lower resolving powers have an exponential penalty as bright atmospheric lines mix into dark spectral channels. Changes from nominal balloon altitude  $h_{\text{CBE}} = 36$  km result in  $NEP \propto 0.15 \exp(-11.8(h/h_{\text{CBE}} - 1)) + 0.85$ , driven by changes in pressure broadening, thus sharing a form similar to spectral resolving power. In this case, NEP plateaus at 0.85 from the upper atmospheric layers in the model<sup>85</sup> and as  $R = 512$  is less able to resolve the narrower atmospheric lines. Stray light at a constant power  $P_{\text{stray}}$  across all detectors results in  $NEP \propto (1 + P_{\text{stray}}/0.25 \text{ fW})^{0.41}$ . Optical ghosts at linear amplitude  $\alpha_{\text{ghost}}$  in the 2D parallel-plate waveguide region can reflect bright atmospheric line radiation into dark channels and results in  $NEP \propto (1 + (\alpha_{\text{ghost}}/3 \times 10^{-4}))^{0.42}$ . Here  $\alpha_{\text{ghost}}$  is the fraction of power from one channel that is spread across all other channels uniformly. Both stray light and crosstalk have similar functional forms because they represent analogous physical processes, except that stray light is in power and crosstalk is in fractional deviation. Crosstalk moves power out of bright channels, whereas stray light adds power to all channels. For stray light that overwhelms atmospheric emission, NEP is approximately  $\propto \sqrt{P_{\text{stray}}}$  expected for a shot-noise background limit.

The required noise scales with angular resolution as  $NEI_{\text{sci}} \propto (\theta_{\text{FWHM}}/\theta_{\text{FWHM}}^{\text{CBE}})^{-0.6}$ . Spectrometer yield, integration time, and cosmic ray deadtime enter the required NEI as the square root.

### 7.3 Calibration and Pointing Model Determination in Flight

The gondola's dewar hatch remains closed on the ground (Sec. 6.5), so measurements during balloon float must characterize the integrated instrument's beam and pointing model. Point sources in the science field provide a flux calibration and pointing centroids through characterization in Planck 545 GHz,<sup>163</sup> and targeted planet observations allow a measurement of the beam shape. (The brightest galaxies in the science field have measurable extent in the Planck and EXCLAIM beams, so they can provide centroid and flux but not beam properties.) We will additionally calculate a calibration with Planck using map-space correlation.<sup>164</sup> This section first

develops calibration requirements for science goals and then describes how these are met by point source observations in targeted fields and the primary survey data.

Statistical errors are 4% (CBE) of the brightest expected [CII] signal at  $\sim 200$  kJy/sr, so we target a  $<4\%$  calibration relative to Planck 545 GHz. Note that planetary emission uncertainty of 5% dominates Planck's 545 GHz<sup>165</sup> absolute calibration error of 6.1%. Knowledge of the beam shape determines the ability to recover small spatial scales accurately. For [CII], correlated shot-noise dominates small angular scales, and a target  $<2\%$  determination of beam width results in a  $1\sigma$  shift in the determination of the shot-noise amplitude for the highest expected [CII] brightness. An expansion in multipole space<sup>166</sup> connects ellipticity (defined here as  $1 - \sigma_{\text{minor}}^2 / \sigma_{\text{major}}^2$ ) to the beam transfer function and implies a  $<8\%$  determination of ellipticity for  $1\sigma$  impact in the inferred line brightness. Point source centroids determine the rotation from the star camera to the telescope boresight and register the intensity field relative to the cross-correlation survey. We define a target at 10% of the pixel size ( $<9$  arc sec) to suppress this to a negligible level. Random pointing model noise effectively broadens the beam and is described in Sec. 6.3.

Given the above requirements on beam and pointing knowledge, we use a Monte Carlo noise simulation to assess the beam measurement sensitivity (including amplitude, additive offset, centroid, minor/major axis width, and rotation angle). Uranus has peak surface brightness<sup>167</sup> of 57 MJy/sr and rises at approximately midnight local time, giving constraints per spectral channel of 2.1% in amplitude and 1.5 arc sec centroid, 1.5% width, 3.9% ellipticity, and 3.9% solid angle, which meet the requirements. Neptune is also an ideal calibrator with a peak surface brightness of 24 MJy/sr, rising at  $\sim 10$  pm local time. In the science survey region, extragalactic point sources have a more limited signal to noise, so constraints refer to a continuum beam fit using the full spectrometer. Bright point sources (peak 3 MJy/sr) in the science field provide amplitude constraints to 3.9% and centroid to 1 arc sec.

Mars, Jupiter, and Saturn are very bright in band, and dynamic range performance is not sufficiently understood at this time to forecast main lobe constraints. Mars permits a characterization to  $10^{-4}$  in the beam response (to a radius of 35 arc min in the nominal diffraction-limited beam) and provides a thermal source. Jupiter provides a constraint on the far sidelobes. The Moon will provide constraints on stray light at high angles as a function of separation. We will additionally search for susceptibility to the galactic plane scattering into the extragalactic fields. Monolithic, unobstructed optics eliminate diffraction from telescope components and supports as well as panel gaps or misalignments. Maintaining spill from the primary at  $< -40$  dB also controls reflected paths for response at large angles. The shroud around the optical exit can be modified based on findings in an engineering flight. A calibration emitter in the optics tube acts as a spectral calibration time-transfer standard and provides a liveness test. The bolometer housing will introduce a spectral ripple, but the time transfer standard does not require an absolute reference. [The emitter will also be calibrated against a beam-filling blackbody source in spectrometer characterization (Sec. 3.2.2).]

## 7.4 Future Work

Here we have described EXCLAIM's science goals, the survey and expected outcomes and margins, and the design phase of the mission. The mission implements this design, targeting an engineering flight in fall 2022 and a science flight in fall 2023. The engineering flight targets one spectrometer on-sky to characterize the integrated performance of the receiver and cryogenic telescope. Future publications will describe the implementation, detailed science forecasts, and results from the flight.

## Acknowledgments

EXCLAIM began in April 2019 as a 5-year NASA Astrophysics Research and Analysis (No. APRA 17-APRA17-0077) grant. We would like to acknowledge valuable contributions from reviewers Ari D. Brown, Jay Chervenak, Lyndell Cleaveland, Nicholas Costen, Phil Coulter, Dale Fixsen, Samelys Rodriguez, Peter Shirron, Peter Taraschi, and Frederick Wang. We also would like to acknowledge contributions by interns Ethan Bennett, Gedalia Koehler, and Akhil Singareddy to the flight software (to be described in a future publication), by Henry Grant,

Alex Lamb, Alberto Martinez, Joaquin Matticoli, and Nina Ong to mission design and software, and by Paul Cursey for the initial and ongoing machining work. We would like to thank Sarah Alspaw, CRESST-II (under Award No. 80GSFC21M0002), and the NASA internship program for coordinating internships that have enabled many areas of the work described here.

## References

1. P. Madau and M. Dickinson, “Cosmic star-formation history,” *Annu. Rev. Astron. Astrophys.* **52**, 415–486 (2014).
2. F. Walter et al., “The evolution of the baryons associated with galaxies averaged over cosmic time and space,” *Astrophys. J.* **902**, 111 (2020).
3. J. Salcido et al., “The impact of dark energy on galaxy formation. What does the future of our Universe hold?,” *Mon. Not. R. Astron. Soc.* **477**, 3744–3759 (2018).
4. C. J. Hogan and M. J. Rees, “Spectral appearance of non-uniform gas at high  $z$ ,” *Mon. Not. R. Astron. Soc.* **188**, 791–798 (1979).
5. E. Kovetz et al., “Astrophysics and cosmology with line-intensity mapping,” *Bull. Am. Astron. Soc.* **51**, 101 (2019).
6. F. Bigiel et al., “The star formation law in nearby galaxies on sub-KPC scales,” *Astron. J.* **136**, 2846–2871 (2008).
7. F. Bigiel et al., “A constant molecular gas depletion time in nearby disk galaxies,” *Astrophys. J. Lett.* **730**, L13 (2011).
8. D. J. Fixsen et al., “The spectrum of the extragalactic far-infrared background from the COBE FIRAS observations,” *Astrophys. J.* **508**, 123–128 (1998).
9. S. Duivenvoorden et al., “Have we seen all the galaxies that comprise the cosmic infrared background at  $250 \mu\text{m} \leq \lambda \leq 500 \mu\text{m}$ ?” *Mon. Not. R. Astron. Soc.* **491**, 1355–1368 (2020).
10. K. W. Masui et al., “Measurement of 21 cm brightness fluctuations at  $z:0.8$  in cross-correlation,” *Astrophys. J. Lett.* **763**, L20 (2013).
11. E. R. Switzer et al., “Determination of  $z:0.8$  neutral hydrogen fluctuations using the 21-cm intensity mapping autocorrelation,” *Mon. Not. R. Astron. Soc.* **434**, L46–L50 (2013).
12. C. J. Anderson et al., “Low-amplitude clustering in low-redshift 21-cm intensity maps cross-correlated with 2dF galaxy densities,” *Mon. Not. R. Astron. Soc.* **476**, 3382–3392 (2018).
13. R. A. C. Croft et al., “Intensity mapping with SDSS/BOSS Lyman- $\alpha$  emission, quasars, and their Lyman- $\alpha$  forest,” *Mon. Not. R. Astron. Soc.* **481**, 1320–1336 (2018).
14. S. Yang, A. R. Pullen, and E. R. Switzer, “Evidence for C II diffuse line emission at redshift  $Z \sim 2.6$ ,” *Mon. Not. R. Astron. Soc.* **489**, L53–L57 (2019).
15. E. R. Switzer et al., “Intensity mapping in the presence of foregrounds and correlated continuum emission,” *Astrophys. J.* **872**, 82 (2019).
16. E. R. Switzer, “Tracing the cosmological evolution of stars and cold gas with CMB spectral surveys,” *Astrophys. J.* **838**, 82 (2017).
17. A. Witzemann et al., “Simulated multitracer analyses with H I intensity mapping,” *Mon. Not. R. Astron. Soc.* **485**, 5519–5531 (2019).
18. T. M. Oxholm and E. R. Switzer, “Intensity mapping without cosmic variance,” *Phys. Rev. D* **104**, 083501 (2021).
19. L. Wolz, C. Blake, and J. S. B. Wyithe, “Determining the H I content of galaxies via intensity mapping cross-correlations,” *Mon. Not. R. Astron. Soc.* **470**, 3220–3226 (2017).
20. G. K. Keating et al., “COPSS II: the molecular gas content of ten million cubic megaparsecs at redshift  $z:3$ ,” *Astrophys. J.* **830**, 34 (2016).
21. B. D. Uzgil et al., “The ALMA Spectroscopic Survey in the HUDF: constraining cumulative CO emission at  $1 \lesssim z \lesssim 4$  with power spectrum analysis of ASPECS LP data from 84 to 115 GHz,” *Astrophys. J.* **887**, 37 (2019).
22. G. K. Keating et al., “An intensity mapping detection of aggregate CO line emission at 3 mm,” *Astrophys. J.* **901**, 141 (2020).
23. G. Popping et al., “The ALMA spectroscopic survey in the HUDF: the molecular gas content of galaxies and tensions with IllustrisTNG and the Santa Cruz SAM,” *Astrophys. J.* **882**, 137 (2019).

24. B. Diemer et al., “Atomic and molecular gas in IllustrisTNG galaxies at low redshift,” *Mon. Not. R. Astron. Soc.* **487**, 1529–1550 (2019).
25. R. Decarli et al., “ALMA spectroscopic survey in the hubble ultra deep field: CO luminosity functions and the evolution of the cosmic density of molecular gas,” *Astrophys. J.* **833**, 69 (2016).
26. S. Yang et al., “Multitracer cosmological line intensity mapping mock light-cone simulation,” *Astrophys. J.* **911**, 132 (2021).
27. M. Silva et al., “Prospects for detecting C II emission during the Epoch of reionization,” *Astrophys. J.* **806**, 209 (2015).
28. A. R. Pullen et al., “Search for C II emission on cosmological scales at redshift  $Z:26$ ,” *Mon. Not. R. Astron. Soc.* **478**, 1911–1924 (2018).
29. H. Padmanabhan, “Constraining the evolution of [C II] intensity through the end stages of reionization,” *Mon. Not. R. Astron. Soc.* **488**, 3014–3023 (2019).
30. A. Zanella et al., “The [C II] emission as a molecular gas mass tracer in galaxies at low and high redshifts,” *Mon. Not. R. Astron. Soc.* **481**, 1976–1999 (2018).
31. S. Alam et al., “Completed SDSS-IV extended Baryon Oscillation Spectroscopic Survey: cosmological implications from two decades of spectroscopic surveys at the Apache Point Observatory,” *Phys. Rev. D* **103**, 083533 (2021).
32. M. Righi, C. Hernández-Monteagudo, and R. A. Sunyaev, “Carbon monoxide line emission as a CMB foreground: tomography of the star-forming universe with different spectral resolutions,” *Astron. Astrophys.* **489**, 489–504 (2008).
33. A. Lidz et al., “Intensity mapping with carbon monoxide emission lines and the redshifted 21 cm Line,” *Astrophys. J.* **741**, 70 (2011).
34. E. Visbal, H. Trac, and A. Loeb, “Demonstrating the feasibility of line intensity mapping using mock data of galaxy clustering from simulations,” *J. Cosmol. Astropart. Phys.* **2011**, 010 (2011).
35. A. R. Pullen et al., “Cross-correlations as a cosmological carbon monoxide detector,” *Astrophys. J.* **768**, 15 (2013).
36. T. Y. Li et al., “Connecting CO intensity mapping to molecular gas and star formation in the epoch of galaxy assembly,” *Astrophys. J.* **817**, 169 (2016).
37. G. Popping et al., “Sub-mm emission line deep fields: CO and [C II] luminosity functions out to  $z = 6$ ,” *Mon. Not. R. Astron. Soc.* **461**, 93–110 (2016).
38. H. Padmanabhan, “Constraining the CO intensity mapping power spectrum at intermediate redshifts,” *Mon. Not. R. Astron. Soc.* **475**, 1477–1484 (2018).
39. S. Yang et al., “An empirical representation of a physical model for the ISM [CII], CO, and [CI] emission at redshift  $1 \leq z \leq 9$ ,” arXiv:2108.07716 (2021).
40. Y. Gong et al., “Intensity mapping of the [C II] fine structure line during the epoch of reionization,” *Astrophys. J.* **745**, 49 (2012).
41. B. Yue et al., “Intensity mapping of [C II] emission from early galaxies,” *Mon. Not. R. Astron. Soc.* **450**, 3829–3839 (2015).
42. G. Popping, R. S. Somerville, and S. C. Trager, “Evolution of the atomic and molecular gas content of galaxies,” *Mon. Not. R. Astron. Soc.* **442**, 2398–2418 (2014).
43. R. S. Somerville, G. Popping, and S. C. Trager, “Star formation in semi-analytic galaxy formation models with multiphase gas,” *Mon. Not. R. Astron. Soc.* **453**, 4337–4367 (2015).
44. G. Popping et al., “The art of modelling CO, [C I], and [C II] in cosmological galaxy formation models,” *Mon. Not. R. Astron. Soc.* **482**, 4906–4932 (2019).
45. R. K. Sheth, H. J. Mo, and G. Tormen, “Ellipsoidal collapse and an improved model for the number and spatial distribution of dark matter haloes,” *Mon. Not. R. Astron. Soc.* **323**, 1–12 (2001).
46. E. R. Switzer et al., “Interpreting the unresolved intensity of cosmologically redshifted line radiation,” *Astrophys. J.* **815**, 51 (2015).
47. M. G. Burton et al., “Extended carbon line emission in the galaxy: searching for dark molecular gas along the G328 sightline,” *Astrophys. J.* **811**, 13 (2015).
48. M. G. Wolfire, D. Hollenbach, and C. F. McKee, “The dark molecular gas,” *Astrophys. J.* **716**, 1191–1207 (2010).

49. F. Valentino et al., “The properties of the interstellar medium of galaxies across time as traced by the neutral atomic carbon [C I],” *Astrophys. J.* **890**, 24 (2020).
50. Collaboration Planck, et al., “Planck 2013 results. XIII. Galactic CO emission,” *Astron. Astrophys.* **571**, A13 (2014).
51. J. Singal et al., “The ARCADE 2 instrument,” *Astrophys. J.* **730**, 138 (2011).
52. N. N. Gandilo et al., “The primordial inflation polarization explorer (PIPER),” *Proc. SPIE* **9914**, 99141J (2016).
53. A. Kogut et al., “Superfluid liquid helium control for the primordial inflation polarization explorer balloon payload,” *Rev. Sci. Instrum.* **92**(6), 064501 (2021).
54. G. Cataldo et al., “Micro-Spec: an ultracompact, high-sensitivity spectrometer for far-infrared and submillimeter astronomy,” *Appl. Opt.* **53**, 1094 (2014).
55. O. Noroozian et al., “Micro-Spec: an efficient compact integrated spectrometer for sub-millimeter astrophysics,” in *26th Int. Symp. Space Terahertz Technol.* (2015).
56. E. M. Barrentine et al., “Design and performance of a high resolution  $\mu$ -Spec: an integrated sub-millimeter spectrometer,” *Proc. SPIE* **9914**, 99143O (2016).
57. M. Mirzaei et al., “ $\mu$ -Spec spectrometers for the EXCLAIM instrument,” *Proc. SPIE* **11453**, 114530M (2020).
58. C. L. Carilli and F. Walter, “Cool gas in high-redshift galaxies,” *Annu. Rev. Astron. Astrophys.* **51**, 105–161 (2013).
59. R. Dünner et al., “The Atacama cosmology telescope: data characterization and map-making,” *Astrophys. J.* **762**, 10 (2013).
60. Dark Energy Survey Collaboration et al., “The dark energy survey: more than dark energy: an overview,” *Mon. Not. R. Astron. Soc.* **460**, 1270–1299 (2016).
61. H. Aihara et al., “Second data release of the Hyper Suprime-Cam Subaru Strategic Program,” *Publ. Astron. Soc. Jpn.* **71**, 114 (2019).
62. D. T. Chung et al., “Cross-correlating carbon monoxide line-intensity maps with spectroscopic and photometric galaxy surveys,” *Astrophys. J.* **872**, 186 (2019).
63. C. Papovich et al., “The spitzer-HETDEX exploratory large-area survey,” *Astrophys. J. Suppl.* **224**, 28 (2016).
64. M. P. Viero et al., “The Herschel Stripe 82 Survey (HerS): maps and early catalog,” *Astrophys. J. Suppl.* **210**, 22 (2014).
65. A. Kogut et al., “The balloon-borne cryogenic telescope testbed mission: bulk cryogen transfer at 40 km altitude,” *Rev. Sci. Instrum.* **91**, 124501 (2020).
66. T. Essinger-Hileman et al., “Optical design of the experiment for cryogenic large-aperture intensity mapping (EXCLAIM),” *Proc. SPIE* **11453**, 114530H (2020).
67. R. Datta et al., “Large-aperture wide-bandwidth antireflection-coated silicon lenses for millimeter wavelengths,” *Appl. Opt.* **52**, 8747 (2013).
68. R. Takaku et al., “Broadband, millimeter-wave anti-reflective structures on sapphire ablated with femto-second laser,” *J. Appl. Phys.* **128**, 225302 (2020).
69. R. Takaku et al., “A large diameter millimeter-wave low-pass filter made of alumina with laser ablated anti-reflection coating,” arXiv:2109.15319 (2021).
70. Q. Wen et al., “Picosecond laser ablation of millimeter-wave subwavelength structures on alumina and sapphire,” *Opt. Laser Technol.* **142**, 107207 (2021).
71. J. Lau et al., “Millimeter-wave antireflection coating for cryogenic silicon lenses,” *Appl. Opt.* **45**, 3746–3751 (2006).
72. C. Dragone and D. C. Hogg, “The radiation pattern and impedance of offset and symmetrical near-field Cassegrainian and Gregorian antennas,” *IEEE Trans. Antennas Propag.* **22**, 472–475 (1974).
73. Y. Mizugutch, M. Akagawa, and H. Yokoi, “Offset dual reflector antenna,” in *IEEE Int. Symp. Antennas and Propag. Digest*, pp. 2–5 (1976).
74. T. Essinger-Hileman et al., “Aerogel scattering filters for cosmic microwave background observations,” *Appl. Opt.* **59**, 5439 (2020).
75. P. A. R. Ade et al., “A review of metal mesh filters,” *Proc. SPIE* **6275**, 62750U (2006).
76. E. R. Switzer et al., “Sub-Kelvin cooling for two kilopixel bolometer arrays in the PIPER receiver,” *Rev. Sci. Instrum.* **90**, 095104 (2019).

77. G. Pisano et al., “Thermal illuminators for far-infrared and submillimeter astronomical instruments,” *Appl. Opt.* **44**, 3208–3217 (2005).
78. E. H. Sharp et al., “Stray light suppression in the Goddard IRAM 2-Millimeter Observer (GISMO),” *Proc. SPIE* **8452**, 84523I (2012).
79. D. T. Chuss et al., “A cryogenic thermal source for detector array characterization,” *Rev. Sci. Instrum.* **88**, 104501 (2017).
80. M. D. Perrin et al., “Simulating point spread functions for the James Webb Space Telescope with WebbPSF,” *Proc. SPIE* **8442**, 84423D (2012).
81. E. S. Douglas and M. D. Perrin, “Accelerated modeling of near and far-field diffraction for coronagraphic optical systems,” *Proc. SPIE* **10698**, 106982U (2018).
82. R. G. Wenzel, J. M. Telle, and J. L. Carlsten, “Fresnel diffraction in an optical system containing lenses,” *J. Opt. Soc. Am. A* **3**, 838–842 (1986).
83. E. J. Wollack et al., “Infrared properties of high-purity silicon,” *Opt. Lett.* **45**, 4935 (2020).
84. J. J. Bock et al., “Emissivity measurements of reflective surfaces at near-millimeter wavelengths,” *Appl. Opt.* **34**, 4812–4816 (1995).
85. S. Paine, “The am atmospheric model,” Zenodo (2019).
86. D. S. Swetz et al., “Overview of the Atacama cosmology telescope: receiver, instrumentation, and telescope systems,” *Astrophys. J. Suppl.* **194**, 41 (2011).
87. J. J. A. Baselmans et al., “A kilo-pixel imaging system for future space based far-infrared observatories using microwave kinetic inductance detectors,” *Astron. Astrophys.* **601**, A89 (2017).
88. G. Cataldo et al., “Second-generation design of Micro-Spec: a medium-resolution, submillimeter-wavelength spectrometer-on-a-chip,” *J. Low Temp. Phys.* **193**, 923–930 (2018).
89. G. Cataldo et al., “Second-generation Micro-Spec: a compact spectrometer for far-infrared and submillimeter space missions,” *Acta Astron.* **162**, 155–159 (2019).
90. C. J. Galbraith and G. M. Rebeiz, “Higher order cochlea-like channelizing filters,” *IEEE Trans. Microwave Theory Tech.* **56**, 1675–1683 (2008).
91. K. U-Yen, K. Rostem, and E. J. Wollack, “Modeling strategies for superconducting microstrip transmission line structures,” *IEEE Trans. Appl. Supercond.* **28**, 1 (2018).
92. J. Ruze, “Antenna tolerance theory: a review,” *IEEE Proc.* **54**, 633–640 (1966).
93. J. D. Wheeler et al., “Antireflection coatings for submillimeter silicon lenses,” *Proc. SPIE* **9153**, 91532Z (2014).
94. A. Gatesman et al., “An anti-reflection coating for silicon optics at terahertz frequencies,” *IEEE Microwave Guided Wave Lett.* **10**(7), 264–266 (2000).
95. C. D. Munson et al., “Composite reflective/absorptive IR-blocking filters embedded in metamaterial antireflection-coated silicon,” *Appl. Opt.* **56**, 5349 (2017).
96. M. J. Myers et al., “Antenna-coupled bolometer arrays for measurement of the cosmic microwave background polarization,” *J. Low Temp. Phys.* **151**, 464–470 (2008).
97. E. Perret et al., “Complex permittivity characterization of benzocyclobutene for terahertz applications,” *Microelectron. Eng.* **85**(11), 2276–2281 (2008).
98. H. M. Heiliger et al., “Low-dispersion thin-film microstrip lines with cyclotene (benzocyclobutene) as dielectric medium,” *Appl. Phys. Lett.* **70**, 2233–2235 (1997).
99. B. T. Bulcha et al., “Electromagnetic design of a magnetically coupled spatial power combiner,” *J. Low Temp. Phys.* **193**, 777–785 (2018).
100. J. Bardeen, L. N. Cooper, and J. R. Schrieffer, “Microscopic theory of superconductivity,” *Phys. Rev.* **106**, 162–164 (1957).
101. S. Gordon et al., “An open source, FPGA-based LeKID readout for BLAST-TNG: pre-flight results,” *J. Astron. Instrum.* **5**, 1641003 (2016).
102. A. Patel et al., “Fabrication of MKIDS for the MicroSpec spectrometer,” *IEEE Trans. Appl. Supercond.* **23**, 2400404 (2013).
103. A. D. Brown and A. A. Patel, “High precision metal thin film liftoff technique,” US Patent 9,076,658 (2015).
104. E. V. Loewenstein, D. R. Smith, and R. L. Morgan, “Optical constants of far infrared materials. 2: Crystalline solids,” *Appl. Opt.* **12**, 398 (1973).

105. M. N. Afsar and H. Chi, “Millimeter wave complex refractive index, complex dielectric permittivity and loss tangent of extra high purity and compensated silicon,” *Int. J. Infrared Millimeter Waves* **15**, 1181–1188 (1994).
106. J. Zmuidzinas, “Superconducting microresonators: physics and applications,” *Annu. Rev. Condens. Matter Phys.* **3**(1), 169–214 (2012).
107. R. B. Pettit and J. Silcox, “Film structure and enhanced superconductivity in evaporated aluminum films,” *Phys. Rev. B* **13**, 2865–2872 (1976).
108. S. Masi et al., “Kinetic inductance detectors for the OLIMPO experiment: in-flight operation and performance,” *J. Cosmol. Astropart. Phys.* **2019**, 003 (2019).
109. J. C. Mather et al., “Calibrator design for the COBE far-infrared absolute spectrophotometer (FIRAS),” *Astrophys. J.* **512**, 511–520 (1999).
110. P. J. Shirron et al., “Design and on-orbit operation of the soft x-ray spectrometer adiabatic demagnetization refrigerator on the Hitomi observatory,” *J. Astron. Telesc. Instrum. Syst.* **4**, 021403 (2018).
111. E. J. Wollack et al., “Impedance matched absorptive thermal blocking filters,” *Rev. Sci. Instrum.* **85**, 034702 (2014).
112. J. Baselmans et al., “Ultra low background cryogenic test facility for far-infrared radiation detectors,” *J. Low Temp. Phys.* **167**, 360–366 (2012).
113. H. Johnson and M. Graham, *High-Speed Digital Design: A Handbook of Black Magic*, Prentice Hall Modern Semiconductor Design, Prentice Hall (1993).
114. A. K. Sinclair et al., “On the development of a reconfigurable readout for superconducting arrays,” *Proc. SPIE* **11453**, 114531T (2020).
115. G. W. Wilson et al., “The TolTEC camera: an overview of the instrument and in-lab testing results,” *Proc. SPIE* **11453**, 1145302 (2020).
116. I. Lowe et al., “Characterization, deployment, and in-flight performance of the BLAST-TNG cryogenic receiver,” *Proc. SPIE* **11453**, 1145304 (2020).
117. G. Presta et al., “The first flight of the OLIMPO experiment: instrument performance,” *J. Phys. Conf. Ser.* **1548**, 012018 (2020).
118. <https://www.lownoisefactory.com/>.
119. <https://www.amuneal.com/>.
120. <https://www.ansys.com/products/electronics/ansys-maxwell>.
121. D. Flanigan et al., “Magnetic field dependence of the internal quality factor and noise performance of lumped-element kinetic inductance detectors,” *Appl. Phys. Lett.* **109**, 143503 (2016).
122. S. Krinner et al., “Engineering cryogenic setups for 100-qubit scale superconducting circuit systems,” *EPJ Quantum Technol.* **6**(1), 2 (2019).
123. A. L. Woodcraft and A. Gray, “A low temperature thermal conductivity database,” *AIP Conf. Ser.* **1185**, 681–684 (2009).
124. <https://www.techapps.com/>.
125. R. C. Dhuley et al., “Thermal conductance characterization of a pressed copper rope strap between 0.13 K and 10 K,” *Cryogenics* **86**, 17–21 (2017).
126. <https://www.clearwatercomposites.com/>.
127. A. Kushino et al., “Thermal conductance and high-frequency properties of cryogenic normal or superconducting semi-rigid coaxial cables in the temperature range of 1–8 K,” *J. Low Temp. Phys.* **193**, 611–617 (2018).
128. G. Ventura and V. Martelli, “Very low temperature thermal conductivity of Kevlar 49,” *Cryogenics* **49**, 376–377 (2009).
129. M. O. Kimball et al., “Low-power, fast-response active gas-gap heat switches for low temperature applications,” *Mater. Sci. Eng. Conf. Ser.* **101**, 012157 (2015).
130. J. A. Rayne, “The heat capacity of copper below 4.2 K,” *Aust. J. Phys.* **9**, 189 (1956).
131. R. C. Zeller and R. O. Pohl, “Thermal conductivity and specific heat of noncrystalline solids,” *Phys. Rev. B* **4**, 2029–2041 (1971).
132. M. Hofacker and H. V. Löhneysen, “Low temperature thermal properties of crystalline quartz after electron irradiation,” *Z. Phys. B: Condens. Matter* **42**, 291–296 (1981).

133. S. Nakamura et al., “Specific heat, thermal conductivity, and magnetic susceptibility of cyanate ester resins: an alternative to commonly used epoxy resins,” *Cryogenics* **95**, 76–81 (2018).
134. M. G. Alexander, D. P. Goshorn, and D. G. Onn, “Low-temperature specific heat of the graphite intercalation compounds KC8, CsC8, RbC8, and their parent highly oriented pyrolytic graphite,” *Phys. Rev. B* **22**, 4535–4542 (1980).
135. J. A. Rayne, “Heat capacity of  $\alpha$  brasses below 4.2 k,” *Phys. Rev.* **108**, 22–25 (1957).
136. S. A. Elrod, J. R. Miller, and L. Dresner, *The Specific Heat of NbTi from 0 to 7 T Between 4.2 and 20 K*, pp. 601–610. Springer US, Boston, Massachusetts (1982).
137. P. Duthil, “Material properties at low temperature,” in *CERN Accelerator School: Superconductivity for Accelerators*, Erice, Italy, R. Bailey, Ed., pp. 77–95 (2014).
138. C. Hagmann and P. L. Richards, “Specific heat of stainless steel below  $T = 1$  K,” *Cryogenics* **35**, 345–345 (1995).
139. S. Chase, L. Kenny, and E. Ronson, “Study of uniformity and reproducibility in the performance of helium-4 sorption coolers,” *J. Low Temp. Phys.* **199**, 1148–1157 (2020).
140. P. J. Shirron, “Applications of the magnetocaloric effect in single-stage, multi-stage and continuous adiabatic demagnetization refrigerators,” *Cryogenics* **62**, 130–139 (2014).
141. R. Datta et al., “Anti-reflection coated vacuum window for the primordial inflation polarization explorer (PIPER) balloon-borne instrument,” *Rev. Sci. Instrum.* **92**, 035111 (2021).
142. <https://www.henkel-adhesives.com>.
143. <https://www.saftbatteries.com/>.
144. “Consolidated Instrument Package (CIP) interface handbook,” <https://www.csbf.nasa.gov/documents/conventional/EC-200-90-H.D.pdf> (2016).
145. G. Coppi et al., “In-flight performance of the BLAST-TNG telescope platform,” *Proc. SPIE* **11445**, 1144526 (2020).
146. N. N. Gandilo et al., “Attitude determination for balloon-borne experiments,” *Proc. SPIE* **9145**, 91452U (2014).
147. N. J. Nigro et al., “Generalized math model for simulation of high-altitude balloon systems,” *J. Aircraft* **22**(8), 697–704 (1985).
148. D. J. Fixsen et al., “A balloon-borne millimeter-wave telescope for cosmic microwave background anisotropy measurements,” *Astrophys. J.* **470**, 63 (1996).
149. E. Di Dio et al., “The CLASSgal code for relativistic cosmological large scale structure,” *J. Cosmol. Astropart. Phys.* **2013**, 044 (2013).
150. A. R. Pullen, O. Doré, and J. Bock, “Intensity mapping across cosmic times with the Ly $\alpha$  line,” *Astrophys. J.* **786**, 111 (2014).
151. A. Loureiro et al., “Cosmological measurements from angular power spectra analysis of BOSS DR12 tomography,” *Mon. Not. R. Astron. Soc.* **485**, 326–355 (2019).
152. H. Guo et al., “Redshift-space clustering of SDSS galaxies: luminosity dependence, halo occupation distribution, and velocity bias,” *Mon. Not. R. Astron. Soc.* **453**, 4369–4384 (2015).
153. M. Manera et al., “The clustering of galaxies in the SDSS-III Baryon Oscillation Spectroscopic Survey: mock galaxy catalogues for the low-redshift sample,” *Mon. Not. R. Astron. Soc.* **447**, 437–445 (2015).
154. B. Reid et al., “SDSS-III Baryon Oscillation Spectroscopic Survey data release 12: galaxy target selection and large-scale structure catalogues,” *Mon. Not. R. Astron. Soc.* **455**, 1553–1573 (2016).
155. S. Eftekharzadeh et al., “Clustering of intermediate redshift quasars using the final SDSS III-BOSS sample,” *Mon. Not. R. Astron. Soc.* **453**, 2780–2799 (2015).
156. J. Gao et al., “A semiempirical model for two-level system noise in superconducting micro-resonators,” *Appl. Phys. Lett.* **92**, 212504 (2008).
157. T. Crawford, “Power spectrum sensitivity of raster-scanned CMB experiments in the presence of  $1/f$  noise,” *Phys. Rev. D* **76**, 063008 (2007).
158. G. Cataldo et al., “Overview and status of EXCLAIM, the experiment for cryogenic large-aperture intensity mapping,” *Proc. SPIE* **11445**, 1144524 (2020).
159. P. A. R. Ade et al., “The experiment for cryogenic large-aperture intensity mapping (EXCLAIM),” *J. Low Temp. Phys.* **199**, 1027–1037 (2020).

160. J. Asorey et al., “Recovering 3D clustering information with angular correlations,” *Mon. Not. R. Astron. Soc.* **427**, 1891–1902 (2012).
161. A. Nicola et al., “Three-dimensional spherical analyses of cosmological spectroscopic surveys,” *Phys. Rev. D* **90**, 063515 (2014).
162. F. Lanusse, A. Rassat, and J. L. Starck, “3D galaxy clustering with future wide-field surveys: advantages of a spherical Fourier-Bessel analysis,” *Astron. Astrophys.* **578**, A10 (2015).
163. Collaboration Planck et al., “Planck 2015 results. XXVI. The second Planck catalogue of compact sources,” *Astron. Astrophys.* **594**, A26 (2016).
164. B. Bertinourt et al., “Comparison of absolute gain photometric calibration between Planck/HFI and Herschel/SPIRE at 545 and 857 GHz,” *Astron. Astrophys.* **588**, A107 (2016).
165. Collaboration Planck et al., “Planck 2015 results. VIII. High frequency instrument data processing: calibration and maps,” *Astron. Astrophys.* **594**, A8 (2016).
166. P. Fosalba, O. Doré, and F. R. Bouchet, “Elliptical beams in CMB temperature and polarization anisotropy experiments: an analytic approach,” *Phys. Rev. D* **65**, 063003 (2002).
167. Collaboration Planck et al., “Planck intermediate results. LII. Planet flux densities,” *Astron. Astrophys.* **607**, A122 (2017).

Biographies of the authors are not available.